Spatially resolved correlative microscopy and microbial identification reveal dynamic depth- and mineral-dependent anabolic activity in salt marsh sediment

Jeffrey Marlow [ID],[1†] Rachel Spietz [ID],[2]
Keun-Young Kim,[3] Mark Ellisman,[3,4] Peter Girguis [ID][1]
and Roland Hatzenpichler [ID][2*]

[1]*Department of Organismic and Evolutionary Biology, Harvard University, 16 Divinity Ave, Cambridge, Massachusetts, 02138.*
[2]*Department of Chemistry and Biochemistry, Department of Microbiology and Cell Biology, Thermal Biology Institute, and Center for Biofilm Engineering, Montana State University, Bozeman, Montana, 59717.*
[3]*Department of Neurosciences, University of California at San Diego School of Medicine and National Center for Microscopy and Imaging Research, University of California, San Diego, La Jolla, California, 92093.*
[4]*Department of Pharmacology, University of California, San Diego, La Jolla, California, 92161.*

Summary

Coastal salt marshes are key sites of biogeochemical cycling and ideal systems in which to investigate the community structure of complex microbial communities. Here, we clarify structural–functional relationships among microorganisms and their mineralogical environment, revealing previously undescribed metabolic activity patterns and precise spatial arrangements within salt marsh sediment. Following 3.7-day *in situ* incubations with a non-canonical amino acid that was incorporated into new biomass, samples were resin-embedded and analysed by correlative fluorescence and electron microscopy to map the microscale arrangements of anabolically active and inactive organisms alongside mineral grains. Parallel sediment samples were examined by fluorescence-activated cell sorting and 16S rRNA gene sequencing to link anabolic activity to taxonomic identity. Both approaches demonstrated a rapid decline in the proportion of anabolically active cells with depth into salt marsh sediment, from ∼60% in the top centimetre to 9.4%–22.4% between 2 and 10 cm. From the top to the bottom, the most prominent active community members shifted from sulfur cycling phototrophic consortia, to putative sulfate-reducing bacteria likely oxidizing organic compounds, to fermentative lineages. Correlative microscopy revealed more abundant (and more anabolically active) organisms around non-quartz minerals including rutile, orthoclase and plagioclase. Microbe–mineral relationships appear to be dynamic and context-dependent arbiters of biogeochemical cycling.

Introduction

Salt marshes are vibrant microbial habitats that play important roles in the biogeochemical cycling of intertidal ecosystems (Tobias and Neubauer, 2019). The confluence of high organic input and seawater-derived sulfate fuel a wide range of carbon, nitrogen, phosphorous and sulfur transformations over compressed spatial scales, leading to abundant, redox-specific niches and microbial communities with high phylogenetic diversity (Lozupone and Knight, 2007; Bowen *et al*., 2012). Because of this, salt marshes represent ideal sites to explore the intricacies of microbial community structure from the microscale to the ecosystem scale.

Within complex microbial communities, spatial relationships are increasingly seen as central determinants of key ecological parameters. In salt marshes, metabolic activity within specific sediment horizons ultimately shapes emergent properties such as carbon sequestration or greenhouse gas emissions (Abdul-Aziz *et al*., 2018; LaRowe *et al*., 2020). More generally, microbe–microbe and microbe–mineral interactions establish evolutionary trajectories (Cordero *et al*., 2012; Andersen *et al*., 2015), niche development (Morton *et al*., 2017), and community structure, function, and stability (Boetius *et al*., 2000; Wright *et al*., 2012; Coyte *et al*., 2015). Furthermore, inter-organism arrangements govern chemical communication (West *et al*., 2007), metabolite exchange (Romine

et al., 2017) and competition for resources (Mitri *et al.*, 2016). Nonetheless, these critical spatial relationships are neglected by the most commonly used methods in microbial ecology such as bulk meta-omics and geochemical approaches. As a result, important metabolic activities may be obscured, including inter-species nutrient cycling (Wilbanks *et al.*, 2014; Cordero and Datta, 2016) and electron transfer to (Lovley and Phillips, 1988; Myers and Nealson, 1988) or from (Shelobolina *et al.*, 2012) specific minerals.

Recent efforts have made progress in analysing microbial communities at the microscale. Nanoscale secondary ion mass spectrometry (nanoSIMS) coupled with stable isotope probing (SIP) and fluorescence *in situ* hybridization (FISH) can resolve anabolic patterns and taxonomically identify individual cells. However, this method typically separates microbial assemblages from their broader environmental context (McGlynn *et al.*, 2015; Musat *et al.*, 2016; Gyngard and Steinhauser, 2019). By combining energy-dispersive X-ray spectroscopy (EDS) with X-ray computed tomography images, Hapca *et al.* extended chemical analyses into a third dimension with resin-embedded soil, but no cellular information was attained (Hapca *et al.*, 2015). Correlative imaging with nanoSIMS and electron and fluorescence microscopy enabled Schlüter *et al.* to pinpoint the position of a subset of the microbial community in relation to leaf fragments, but metabolic activity and microbial identities were not considered (Schlüter *et al.*, 2018). A promising addition to this emerging field is SIP combined with non-destructive Confocal Raman microspectroscopy, which was recently used to measure the *in situ* activity and substrate uptake of microbes in transparent soil microcosms (Sharma *et al.*, 2020).

The work presented here advances this line of microbial ecology research. The methods herein not only preserve spatial arrangements and link cell positions to mineralogy through correlative microscopy, but also establish the presence, location and mineralogical associations of anabolically active cells. Anabolic activity was assessed with bioorthogonal non-canonical amino acid tagging (BONCAT), a next-generation physiology approach (Hatzenpichler *et al.*, 2020) that uses substrate analogue probing to visualize protein synthesis in active cells. A non-canonical amino acid, such as L-homopropargylglycine (HPG) or L-azidohomoalanine, is incorporated into growing peptides by native methionyl-tRNA synthetases. Subsequent azide-alkyne click chemistry allows fluorescent detection of newly synthesized proteins (Sletten and Bertozzi, 2009). BONCAT was initially developed in neuron (Dieterich *et al.*, 2006), eukaryote (Hinz *et al.*, 2011) and cultured bacteria (Hatzenpichler *et al.*, 2014) systems; more

recently, it was optimized for environmental microbial communities and shown to have no measurable effect on community composition or metabolic activity (Hatzenpichler *et al.*, 2014, 2016). The approach has been proven effective in a diverse range of bacterial and archaeal cultures (Hatzenpichler *et al.*, 2014; Hatzenpichler and Orphan, 2015); ocean water (Samo *et al.*, 2014; Leizeaga *et al.*, 2017; Sebastián *et al.*, 2019), marine sediment (Hatzenpichler *et al.*, 2016), hot spring (Reichart *et al.*, 2020), and soil microbiomes (Couradeau *et al.*, 2019); as well as marine viruses and bacteriophages (Pasulka *et al.*, 2018). BONCAT appears to be a taxonomically agnostic measure of anabolic activity that correlates well with other metrics of activity (Bagert *et al.*, 2014; Hatzenpichler *et al.*, 2014, 2020; Samo *et al.*, 2014) with only small effects on metabolism (Steward *et al.*, 2020) and protein chemistry (Bagert *et al.*, 2014; Lehner *et al.*, 2017).

In this study, we mapped the anabolic activity of microorganisms in sediments from Little Sippewissett salt marsh in Falmouth, MA, where terrestrial freshwater runoff, seawater, high organic input, and abundant light and chemical energy lead to dramatic redox stratifications within the top few centimetres of sediment and a wide range of metabolic niches (Wilbanks *et al.*, 2014, 2017; Larsen *et al.*, 2015). Using purpose-built equipment (Fig. 1), we incubated a series of sediment cores with HPG *in situ* for 3.7 days. One core was processed for horizon-specific fluorescence-activated cell sorting (FACS) and 16S rRNA gene amplicon sequencing. A parallel core was used for correlative microscopy; samples were embedded in resin to maintain precise spatial arrangements, sectioned, stained, and analysed using fluorescence and electron microscopy to map active and inactive biomass as well as identifiable mineral grains.

Mineralogical identities of individual grains were assessed in order to determine whether different mineral types corresponded with notable differences in organism abundance, configuration, or anabolic activity. Like the vocabulary used to describe microbe–microbe interactions, microbe–mineral interactions can be harmful, neutral, or beneficial for the organism. Microbial sorption to quartz grains – which are dominant in coastal settings – has been demonstrated, but repellent electrical charges make the interaction less favourable than those with other mineral types (Mills *et al.*, 1994; Gong *et al.*, 2018). The best-studied beneficial interactions are the microbial reduction of iron or manganese oxides (Thamdrup, 2000), which enable bacteria to off-load reducing power, altering mineral structure and chemistry in the process (Kawano and Tomita, 2002; Welch and Banfield, 2002). A number of factors influence the nature of these interactions, including accessible
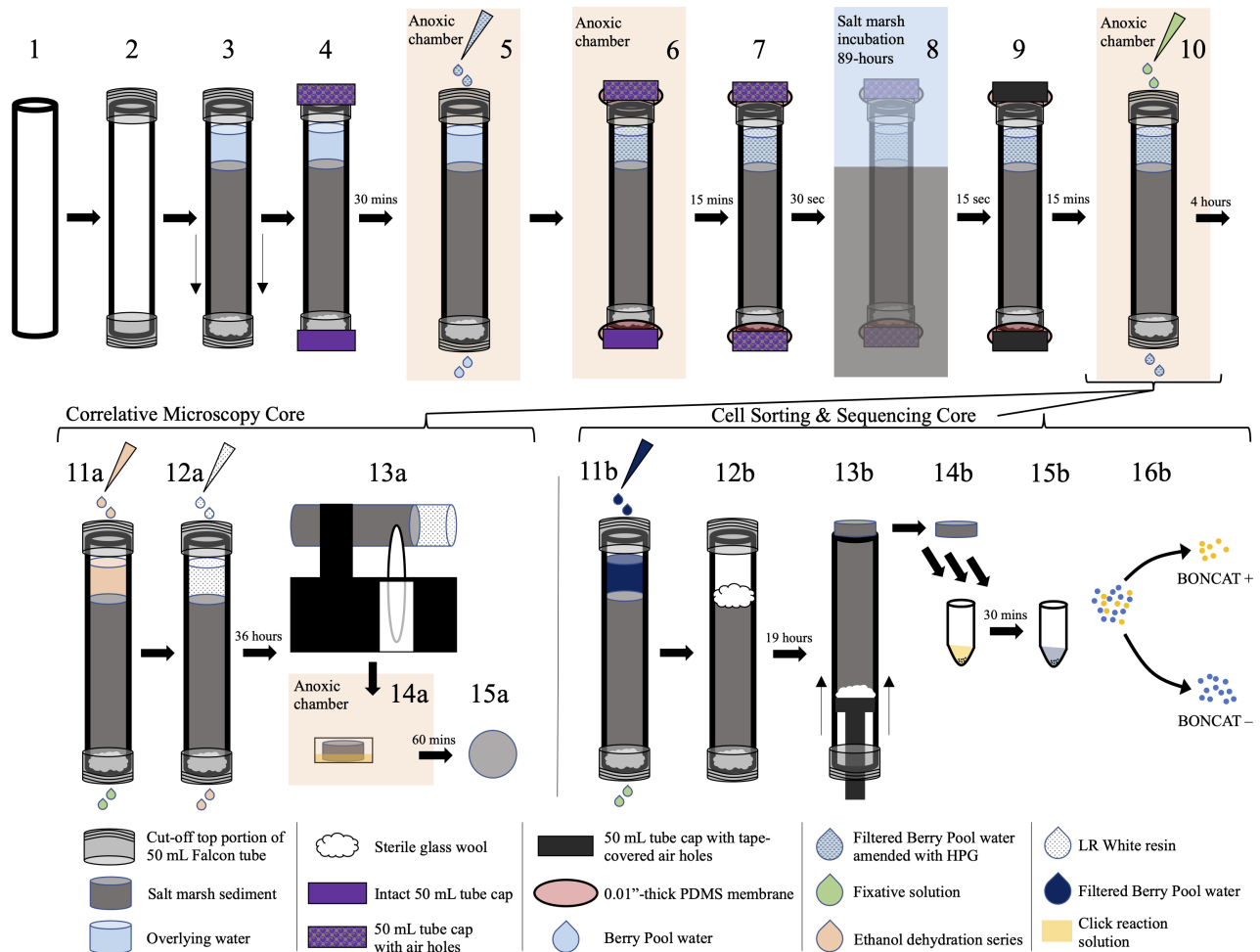
Fig. 1. An overview of the experimental and sample processing approach deployed in this study (components are not to scale; please refer to the text for the correct dimensions). The PETG tube is cut to the appropriate dimensions and the lower edge is bevelled (1). Cut-off 50 ml Falcon tube tops are secured to the PETG tube with epoxy (2), and sediment is collected from the marsh by pressing the tube downward into the sediment (3). A sterile plug of glass wool is added to the bottom to keep the material in place, and the full tube is pulled back out of the sediment. Tube lids are secured; the top lid has a perforated top to allow contact with an oxic atmosphere (4). In an anoxic chamber, lids are removed and fluid is replaced drop-wise by pipette with 50 μM HPG in 0.22 μm-filtered Berry Pool water (5). (Not all cycles of fluid replacement are shown; see text for full protocol.) PDMS membranes are secured to top and bottom of tube with twist-on lids (6). Sample tubes are returned to the marsh; immediately prior to emplacement in the Berry Pool sediment, the bottom lid is perforated to allow gaseous continuity with the environment (7). The sample is placed back in the sediment at the initial collection location for the duration of the incubation period (8); upon recovery, lid perforations are immediately covered with electrical tape to minimize gas exchange during transport back to the lab (9). In the anoxic chamber, incubation fluid is replaced with fixative and incubated for 4 h at room temperature (10). Correlative microscopy cores are processed according to steps 11a-15a. The fixed core is removed from the anoxic chamber and infiltrated with an ethanol dehydration series (11a) followed by LR White resin (12a), which is allowed to cure during a 36 h incubation at 60 °C. The embedded core is then sectioned by a sterile water-cooled diamond saw (13a), and sectioned surfaces are incubated in the click solution for 60 min in the dark in an anoxic chamber (14a). Sample sections are now ready for SYBR green counterstaining and fluorescence and electron microscopy (15a). Cores for cell sorting and sequencing are processed according to steps 11b-16b. Following fixation, the core is rinsed with 0.22 μm-filtered Berry Pool water (11b). The overlying liquid and top 1.0 cm of sediment are removed and replaced by a plug of sterile glass wool for transport (12b). A sterile plunger was used to extrude the core in 1 cm increments (13b). Cells were extracted from these subsamples and then incubated in the click solution for 30 min in the dark (14b). Cells were then washed (15b) and introduced to the cell sorter, which separated BONCAT positive and BONCAT negative cells (16b) for downstream sequencing. [Color figure can be viewed at wileyonlinelibrary.com]

surface area, mineral lattice structure, co-occurrence of organic matter, and other environmental conditions such as temperature and pH (Dong *et al*., 2009). Beyond iron and manganese, microbes have been shown to associate with other cations, acquiring potassium from silicates (Valsami-Jones *et al*., 1998), releasing organic ligands that

adhere to aluminium (Rogers and Bennett, 2004), and using reducing power from photo-catalytically activated titanium oxide (Lu *et al*., 2012). By identifying the mineral grains with which the native microbial community associates, the nature of previously undetected microbe–mineral relationships can be examined in further detail.

The novel approach presented here allowed us to map active and inactive organisms in their native microscale configuration and identify the active and inactive microbial communities in adjacent sediment horizons. Our results indicate that the proportion of anabolically active organisms decreased dramatically below the photic zone and that mineralogy likely has an impact on the relative abundance and anabolic activity of mineral grain-associated organisms. High-throughput 16S rRNA gene sequencing of active and inactive microbial communities in adjacent sediment cores revealed a continuous progression of community structure with depth, oriented around shifting metabolisms of photosynthesis, sulfur cycling and fermentation. Notably, with correlative fluorescence and electron microscopy, we observed differential cell association with distinct mineral types and a greater proportion of organisms inside mineral grains in lower (6–7 cm) sediment horizons compared with shallower zones. While the full potential of microbiome mapping remains to be realized, this benchmarking study unveils a new experimental approach to (i) evaluate how metabolic activity relates to microscale environmental factors, and (ii) develop testable hypotheses regarding metabolic interactions among members of complex microbial communities.

Results and discussion

This study reveals how microbial presence and anabolic activity in salt marsh sediment relate to sediment depth and mineralogical distributions at the microscale with a new level of realism. In this section, we first present results of quality assurance tests to demonstrate the reliability of our newly developed methods before sharing insights on community structure derived from BONCAT-FACS sequencing and findings of spatial arrangements and putative microbe–mineral interactions via correlative microscopy. We close with key insights made possible through the integrated combination of the two newly developed techniques. Experimental treatments and depth-based sampling details for the samples discussed below are provided in Table S1 and Fig. S1 respectively.

Control experiments constrain false positives and cell entrainment

To validate our protocols, control samples were analysed and targeted procedural experiments were performed. The contribution of false-positive 'organism' designations via fluorescence microscopy was quantified by comparing samples BM and AM; both sediment cores were incubated in the presence of 50 μM HPG, but the latter had been autoclave-sterilized, eliminating anabolic activity and the incorporation of HPG into new biomass

(Table S1). Across five fields of view from sample BM's top horizon (7.6 mm depth) and an arbitrary horizon in the homogenized AM core, sample AM exhibited 3.5% as many SYBR-active objects and 3% as many Cy3-active objects as sample BM (Fig. S2). When corrected for the pre-sterilization biomass abundance in sample AM $(9.81 \times 10^8$ cells/cm^3), these apparent false-positive rates increased to 6.9% for SYBR signal and 5.9% for BONCAT signal. Analysis areas contained roughly equivalent proportions of mineral surface area and pore space. Although the comparison between the two samples was not exact – autoclaving could have both denatured photosynthetic pigments and incompletely degraded cells – this analysis suggests that our efforts to constrain background fluorescence or non-specific binding of HPG or the dyes could benefit from future optimization, but false-positive signal did not dramatically influence our results. When comparing the top horizons of samples BM and CM (a live environmental incubation that did not receive HPG), we found that CM had 23% more SYBR-active objects but just 2.9% as many Cy3-active objects as sample BM (or 2.3% as many when normalized by SYBR-active biomass, Table 1; Fig. S2). These data strongly suggest that HPG did not affect SYBR signal but was required for BONCAT signal and that Cy3-active features were not attributable to cellular autofluorescence.

Clarifying the role that our experimental treatment had on the microbial community and the empirical biases that may result was a key priority. Daily fluctuations of the Berry Pool water level, which ranges from ∼5 to 30 cm water depth over the course of a tidal cycle, consistently introduce and remove transient organisms that may not be physically associated with sediment particles. Nonetheless, it is possible that the percolation of fluids through the incubation chambers associated with our protocol might transport microbial cells outside of their naturally occurring habitats. To test this possibility, we introduced 1 ml of 1×10^9 ml^{-1} 1 μm diameter YG carboxylate fluorescent microspheres (Polysciences, Warrington, PA) to the overlying water of a salt marsh sediment core (Sample MM, Table S1). These microspheres are commonly used to simulate microorganism transport and constrain contamination in sediments, soils and subsurface environments (Smith *et al*., 2000; House *et al*., 2003; Goeppert and Goldscheider, 2011; Bang-Andreasen *et al*., 2017; Labonté *et al*., 2017; Daly *et al*., 2018). Following microsphere addition, the core was treated identically to the BM sample through the embedding step (see Experimental procedures section). Throughout the process, flow-through liquid fractions were collected and concentrated on 0.22 μm polycarbonate filters. After embedding, multiple horizons were sectioned and examined with fluorescence microscopy. Bead counts over five representative fields of view at 10.7 mm above the

Table 1. Cell abundance and percentage of anabolically active cells as determined through fluorescence microscopy and BONCAT-FACS analyses.

Fluorescence microscopy analysis				FACS analysis	
	Cell abundance (cells/cm^3)		% Active	% Active	
Sediment depth (mm)	Sample CM	Sample BM		Sample BS	Sediment depth (mm)
7.6	2.4×10^9	1.95×10^9	51.3	70.0	0–10
12	2.46×10^9	2.86×10^9	22.3	22.4	10–20
				21.8	20–30
35.5	3.66×10^8			10.5	30–40
				17.4	40–50
				13.0	50–60
60.7	5.8×10^8	6.85×10^8	12.1	14.5	60–70
				11.5	70–80
				12.8	80–90
				9.4	90–100

Where % active values are available for both fluorescence microscopy and FACS datasets, the linear correlation coefficient was 0.99. Cells with gray shading indicate the absence of data.

sediment–water interface, 2.0 mm depth, 5.3 mm depth, 9.8 mm depth, and 23.3 mm depth (Fig. S3), as well as 16 liquid fractions, were averaged and scaled by the overall cross-sectional area of the core. *Z*-axis transmission of bead fluorescence under confocal microscopy examination was 8.75 μm. Linear interpolation of data points indicated that 99.3% of beads remained above the 7.6 mm horizon, which was the shallowest horizon used for microscopy analysis. Assuming a cell density of 10^6 ml^{-1} in the overlying water and 30 ml of overlying water in the initial core sample, we calculate that 6×10^{-3}% and 8×10^{-4}% of cells detected in the 7.6 and 12 mm horizons respectively, are attributable to entrained surface water cells. Because a horizon lower than 60.7 mm was not examined with the bead test, an analogous figure is not attainable for the 60.7 mm horizon. However, given the trends observed here, we believe the contribution from surface-entrained organisms is negligible. This analysis gave us confidence in interpreting mineral-associated organisms as native to the observed sediment horizons.

BONCAT-FACS illuminates community structure and prominent metabolic functions

Several previous studies have elucidated key aspects of the Little Sippewissett salt marsh microbiological system and its role in biogeochemical cycling (Shapiro *et al.*, 2011; Wilbanks *et al.*, 2014, 2017; Larsen *et al.*, 2015; Salman *et al.*, 2015; Mackey *et al.*, 2017). Because geochemical measurements were not conducted as a part of this study, we leverage this heritage to convey prevailing conditions within different sediment horizons and infer physiological traits based on the 16S rRNA gene data we collected. By incorporating BONCAT-FACS into community analyses of centimetre-thick sediment horizons, we can focus specifically on the anabolically active subset of the community and detect shifting metabolic priorities. Sequence data and relative abundances of assigned lineages for bulk, active and inactive microbial communities across all horizons are reported in Supporting Information Dataset 1.

The top horizon (0–10 mm) of Little Sippewissett salt marsh sediment exhibits dramatic redox gradients as oxygen concentrations fall below detection by 5 mm, sulfide rises from 0 to between 0.5–1.5 mM, and pH drops 1–2 units immediately below the surface before stabilizing at ∼7.0–7.3 at night and ∼6.0 during the day below 4 mm (Salman *et al.*, 2015). Our results showed that the majority of microbes recovered from this horizon via FACS were anabolically active during the incubation (70%, Table 1) and that the community was dominated by the phyla *Proteobacteria* (48% relative abundance) and *Bacteroidetes* (30%), whose metabolically diverse members are suggestive of a range of redox conditions and substantial heterotrophic cycling in the upper sediment layer (Spain *et al.*, 2009; Gómez-Pereira *et al.*, 2012). The prevalence of the purple sulfur bacteria *Thiohalocapsa* (14.4%) and putative sulfate-reducing bacteria *Desulfobulbaceae* (6.5%) in the bulk community were reflective of the abundant 'pink berries' found at the sediment surface (Fig. S4) (Seitz *et al.*, 1993; Wilbanks *et al.*, 2014). *Thiohalocapsa* were substantially less abundant in both the active (3.8%) and inactive sorted cells (2.7%), likely due to incomplete disaggregation during cell extraction (see Experimental procedures section below). *Desulfobulbaceae* were more prevalent in the active community (14.0%) than in the bulk cells (6.5%), suggesting that not all of these sulfate-reducing organisms were syntrophically associated with purple

sulfur bacteria (Dataset 1). Among organisms potentially involved with sulfur-cycling consortia, we observed a more diverse distribution of putative sulfate-reducing bacteria lineages (65 genus-level *Desulfobacterales* amplicon sequence variants, or ASVs) compared with a more streamlined set of purple sulfur bacteria with a single dominant representative (19 genus-level *Chromatiales* ASVs, with *Thiohalocapsa* accounting for 83% of the recovered sequences).

Sequencing of active and inactive communities in the 0–10 mm range revealed eight lineages that each represented >1% of the overall relative abundance that was significantly more abundant in the anabolically active subset (Dataset 1). Of these, six were putative members of the pink berry consortia (*Chromatiales* or *Desulfobacterales* orders), one was a photoheterotroph (*Halieaceae*) that may encode multiple light-harvesting complexes (Spring *et al*., 2015), and one was a member of the metabolically diverse *Rhodobacteraceae* family (Pujalte *et al*., 2014; Pohlner *et al*., 2019). Many of the other abundant inactive lineages – including three putative sulfate reducers and three putative purple sulfur bacteria – were among the most abundant ASVs in both the active and inactive fractions (Dataset 1). This overlap may indicate stochastic activity of particular consortia or a metabolic dependence upon physicochemical traits on a sub-cm scale, such as pore connectivity or identity of neighbouring organisms. Alternatively, our conservative gating approach may have captured some active cells with low fluorescence in the inactive gate (Fig. S5).

In the sediment horizons below 10 mm, oxygen is absent and sulfide concentrations range from ∼0.5 to 2.5 mM. Day or night pH values remain largely consistent with depth to 30 mm, producing values of ∼6.9–7.2 at night, and ∼6.0–6.3 during the day (Salman *et al*., 2015), typical of carbonate-buffered anoxic sediments (Soetaert *et al*., 2007). Under these more energetically constrained conditions, the proportion of active organisms detected by FACS decreased substantially from 70% in the top layer to values between 9.4% and 22.4% in the subsurface horizons (Table 1), signifying a shift from primary production to burial and degradation. The most prominent sulfur-metabolizing orders, *Desulfobacterales* and *Desulfarculales*, accounted for a higher proportion of the anabolically active community – 34.6% ± 3.3% SD and 5.7% ± 1.6% SD respectively, across the nine horizons between 10 and 100 mm – than in the top sediment horizon (25% and 3.6% respectively; Fig. 2). The prominence of these lineages is consistent with previous observations that sulfate reduction is the main metabolism responsible for remineralization of organic matter in salt marsh sediments, accounting for 67%–80% of total respiration in various salt marshes (Howarth and Teal, 1979; Howarth and Giblin, 1983; Howarth and Merkel, 1984) and more

than 90% of primary production degradation at neighbouring Great Sippewissett Marsh (Howarth and Teal, 1979). Members of the most abundant order across all subsurface horizons, *Desulfobacterales*, were more prevalent among anabolically active than inactive organisms, while the *Desulfarculales* frequently exhibited the opposite relationship (Fig. 2). The latter order consisted of the *Desulfatiglans* genus, whose abundance in subseafloor environments has been attributed to its metabolic versatility in the degradation of aromatics (Jochum *et al*., 2018). In the context of the salt marsh, this versatility has seemingly enabled the genus to persist throughout the core, but the cost of a diverse metabolic portfolio could be substantial lag times in metabolic re-routing or extended periods of quiescence for organisms whose metabolic substrate is not present at a given time.

Purple sulfur bacteria of the order *Chromatiales*, as anticipated, comprised a decreasing proportion of active cells down-core in the absence of light. Nonetheless, one *Chromatiaceae* ASV (of the *Halochromatium* genus) was the second most abundant lineage among active organisms between 10 and 20 mm, suggesting that bioturbation late in the incubation contributed to in-mixing from more photosynthetically active surface layers, or that chemotrophic growth occurred *in situ* in microoxic microenvironments (Hell *et al*., 2008; Hunter *et al*., 2008). More broadly, *Chromatiales* was the most abundant order in several inactive fractions, suggesting that purple sulfur bacteria may be among the larger microbial contributors of organic matter to deeper sediments. *Cellvibrionales* and *Rhodobacterales* were found at higher relative abundance in active than inactive fractions at the top of the core, but the opposite was true below 20 mm depth. *Cellvibrionales* have traditionally been considered oligotrophs, but some members of the order contain sulfur oxidation pathways and others can grow photoheterotrophically (Spring *et al*., 2014, 2015); this diversity of environments may explain their relatively consistent presence among both active and inactive sequences throughout the core. *Rhodobacterales* are noted early colonizers of particles (Dang *et al*., 2008); one of the most prominent genera detected throughout the core was *Rubribacterium*, a non-sulfur purple bacterium that is a facultative aerobe (Boldareva *et al*., 2009). These traits help explain the order's presence at all horizons and its decrease in the active fraction with depth. The observed vertical profile of *Pirellulales* sequences is consistent with aerobic chemoorganotrophs (Schlesner *et al.,* 2004) which may have been deposited onto the sediment surface, metabolically inactivated quickly upon burial and the onset of anoxic conditions, and potentially scavenged by the anoxic heterotrophs.

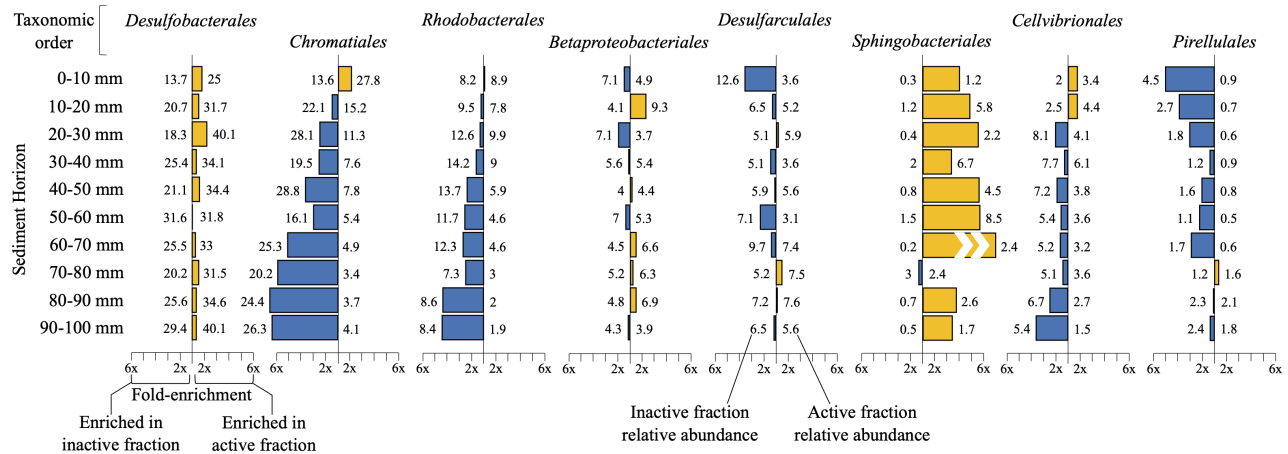Fermentation may be a prominent metabolism in the anoxic horizons we sampled. *Sphingobacteriales* are

Fig. 2. Trends of the relative abundances of active and inactive subsets of the eight most prevalent orders with sediment depth, as detected by BONCAT-FACS combined with 16S rRNA gene sequencing for sample BS. At each horizon, the relative abundance contribution for each order was determined in both the anabolically active sorted cells and the inactive sorted cells. Values to the right of the axis indicate the relative abundance of that order in the active fraction; values to the left indicate the relative abundance in the inactive fraction. The coloured bars reveal if the order was enriched in the active fraction (yellow bars) or the inactive fraction (blue bars) in a given horizon. The length of bars shows fold-enrichment, as indicated by the x-axis, calculated by dividing the larger relative abundance value by the smaller relative abundance value for each order in each sediment horizon. [Color figure can be viewed at wileyonlinelibrary.com]

typically associated with carbon remineralization in oxic soils (Fierer *et al*., 2007), but they do retain fermentation-associated genes (Hester *et al*., 2018) that may explain their presence among the active cell fraction we recovered from below 10 mm depth (Fig. 2). Members of the fermentative *Clostridia* class (Mead, 1971; O'Brien and Ljungdahl, 1972; Winter *et al*., 1987) increased in relative abundance downcore (Pearson's $r = 0.76$, $p < 0.05$), as did their enrichment in the active fraction ($r = 0.79$, $p < 0.01$). In salt marshes, fermentation produces organic acids such as acetate (Gandy and Yoch, 1988; Kostka *et al*., 2002) that may promote syntrophic relationships with the abundant sulfate-reducing bacteria we observe (Ford, 1993; Bahr *et al*., 2005). Few sequences from putative methanogens were observed, potentially due to primer bias (Bahram *et al*., 2019), seasonality (Buckley *et al*., 2008), and the presence of abundant sulfate-reducing bacteria and a range of homoacetogens that may be more successful at attaining hydrogen (Oremland and Polcin, 1982; Ye *et al*., 2014).

Correlative microscopy reveals precise spatial relationships between microbes and minerals

Correlative microscopy analyses at three distinct horizons revealed changes in organism abundance from 1.95×10^9 cm^{-3} at 7.6 mm depth to 2.86×10^9 cm^{-3} at 12 mm depth and 6.85×10^8 cm^{-3} at 60.7 mm depth. Moving downward along these three horizons, the proportion of anabolically active organisms decreased from 51.3% (7.6 mm) to 22.3% (12 mm) to 12.1% (60.7 mm),

a trend that correlated well with BONCAT-FACS data ($R^2 = 0.99$; Table 1).

The uppermost section examined by correlative microscopy was located within the top sequenced horizon, at a depth of 7.6 mm (Fig. 3). In the analysed area, 15 of the 20 mineral grains were quartz (SiO$_2$), while albite (NaAlSi$_3$O$_8$), orthoclase (KAlSi$_3$O$_8$), rutile (TiO$_2$), plagioclase (a solid solution range from NaAlSi$_3$O$_8$ to CaAl$_2$Si$_2$O$_8$) and Ca/K/Mg/Fe silicate grains of indeterminant mineralogy were also observed. 73.4% of cells were associated with (located inside or around) quartz grains (Table 2). However, when cell biomass abundances were normalized by proxies for mineral surface area and volume, non-quartz grains exhibited 33% greater biomass per unit surface area and 43% greater biomass density per unit volume.

Overall, 77.5% of observed cells were outside their associated mineral grains while 22.5% were found inside, frequently along fractures or pores up to several hundred μm^2 in cross-sectional area visible by SEM (see e.g. Fig. 3B). We found that the degree of anabolic activity was higher around non-quartz minerals when compared with quartz-associated cells (Table 2). Although low abundances of these mineral types make generalizations difficult, it is possible that metal cations in the mineral structures facilitate a wider range of metabolic reactions than the more chemically inert quartz (Shi *et al*., 2016). The electrical semi-conductivity of titanium oxide can promote extracellular electron transfer (Zhou *et al*., 2018) and, via photo-catalysis, stimulate the growth of non-phototrophic microbes (Lu *et al*., 2012); these mechanisms may account for the elevated proportion
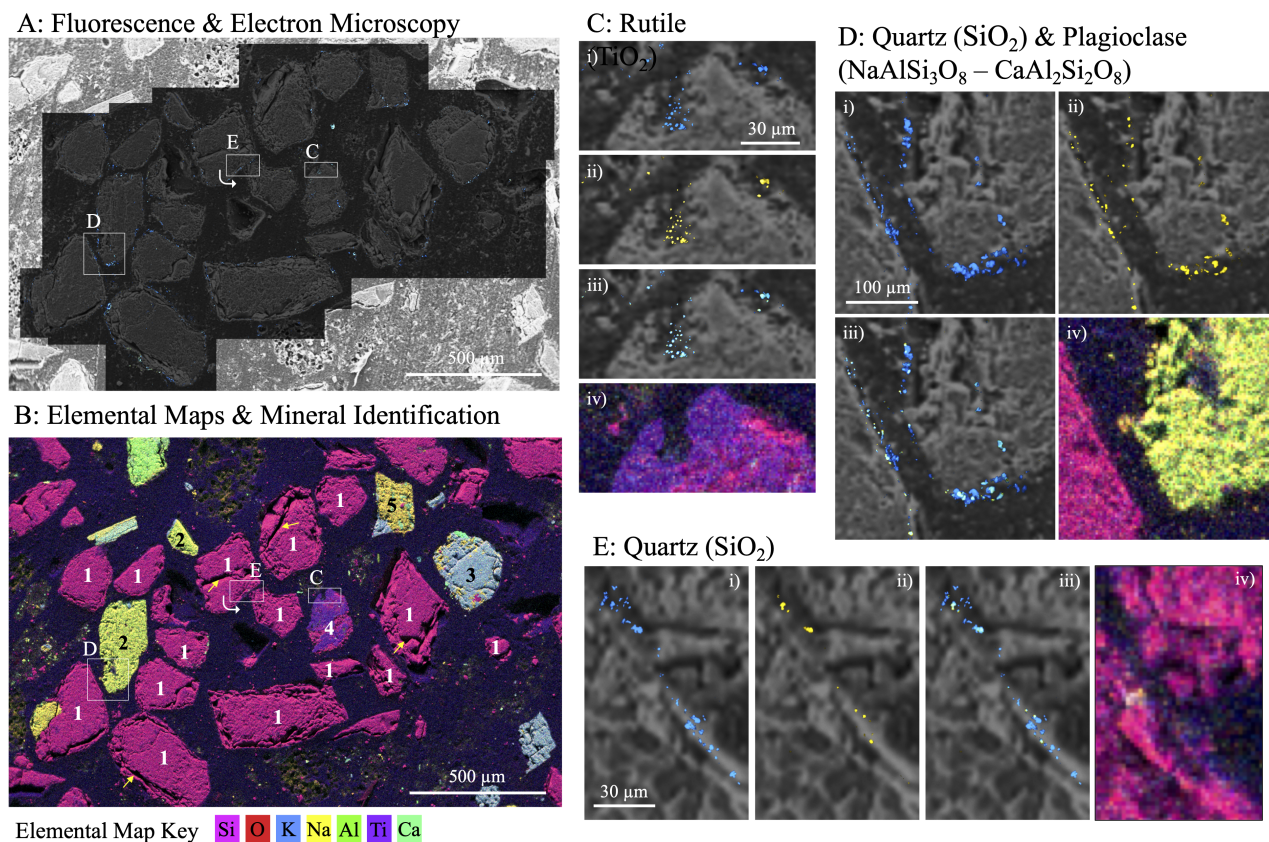
Fig. 3. Correlative fluorescence and electron microscopy from the uppermost section (7.6 mm sediment depth).
A. Overlain on the base SEM image are two fluorescence channels showing SYBR-active features in blue, and BONCAT-active features in yellow. The dark zonation indicates the fluorescence microscopy footprint.
B. Composite elemental maps derived from EDS analysis show the mineral grains that were analysed, labelled by mineral type. 1 = Quartz; 2 = Plagioclase; 3 = Orthoclase; 4 = Rutile; 5 = Albite. Yellow arrows indicate particularly large mineral grain pore spaces for illustrative purposes. C–E show three mineralogically distinct sites in detail. (i) SYBR green, (ii) BONCAT and (iii) merged channels, as well as (iv) EDS elemental abundance maps (in which dark blue background represents the resin). Brightness and contrast of all fluorescence microscopy views have been increased by 40% to enhance signal visibility; original images as presented in the methods can be found at the following Dropbox link: tinyurl.com/4mcw39xu [Color figure can be viewed at wileyonlinelibrary.com]

(78%, compared with a mean of 51.7% for this horizon) of active cells associated with the exterior of the titanium oxide rutile grain.

Within the 10–20 mm depth zone, a post-BONCAT embedded section from a depth of 12 mm was examined by correlative microscopy (Fig. 4). Twenty-two mineral grains were analysed; as above, the vast majority of grains were quartz, and the microbes associated with non-quartz grains (in particular, orthoclase) had a higher proportion of anabolically active constituents (Table 2). Some of the highest concentrations of active cells were associated not with well-defined minerals, but rather with heterogeneous patches that include small particles of quartz, sodium and iron (Fig. 4C). In comparison with larger mineral grain interfaces, these particle assemblages offer greater chemical diversity and more potentially reactive surface area, factors that may facilitate interactions among microbes. The higher surface

roughness associated with particle assemblages may also influence fluid flow through the column, reducing drag and providing more stable microenvironments (Taylor *et al*., 2006).

The deepest section used for correlative microscopy analysis was at a depth of 60.7 mm. Forty-three mineral grains were observed in the fluorescence microscopy field of view, which also contained the highest abundance of small mineral particles and heterogenous patches of the three sections (Fig. 5), potentially due to the degradation processes that accompany burial and longer residence times within the sediment column (Curtis, 1987). Despite the high abundance of associated mineral interfaces across a range of spatial scales, this horizon exhibited the lowest microbial abundance and the lowest proportion of anabolically active organisms. This observation is consistent with commonly observed trends in sediments, where electron acceptor depletion and the

Table 2. Proportions of cells, and the anabolically active subsets, associated with mineral exteriors and interiors at the three horizons examined by correlative microscopy.

		% of associated biomass	% active	Associated biomass per unit surface area	Associated biomass per unit volume	% Outside	% of Outside biomass that was active	% Inside	% of Inside biomass that was active
7.6 mm horizon	All minerals	100	51.3			77.5	51.7	22.5	52.8
	Quartz	73.4	49.7	0.97	0.93	80.6	48.9	19.4	50.1
	Plagioclase	10	62.6	1.3	1.44	75.9	63.6	24.1	59.5
	Orthoclase	6.7	61.2	1.31	1.11	90	60.2	10	64.9
	Rutile	5.3	66	1.26	1.5	42	78	58	57.3
12 mm horizon	All minerals	100	22.3			80.2	20	19.8	24.8
	Quartz	85.6	21.7	0.99	0.94	79.1	19.1	20.9	24.3
	Orthoclase	9.5	29.8	1.24	1.68	89.6	30	10.4	29.8
60.7 mm horizon	All minerals	100	12.1			62.2	10.3	37.8	14.9
	Quartz	62.1	10.3	0.86	0.82	69.5	9.3	30.5	12.5
	Plagioclase	21	12	1.52	1.6	45.6	7.6	54.4	15.6
	Orthoclase	13.5	15	1.39	1.6	55.7	12.9	44.3	17.6

For the biomass per surface area and volume, the relative proportion of biomass associated with a given mineral type was divided by the relative proportion of surface area or volume accounted for by that mineral type. Values less than 1 indicate fewer associated cells than would be expected given an even distribution of biomass across mineral perimeters or surfaces. Only mineral types that accounted for at least 5% of the observed biomass in a given horizon are included in this analysis.

Color shadings are intended to clarify different data categories. Orange cells refer to all observed biomass, blue cells refer to all biomass located outside mineral grains, and green cells refer to all biomass located inside mineral grains.

progressive loss of labile carbon with depth can lead to energetically constrained conditions (Blume *et al*., 2002; Jörgensen *et al*., 2002; Stone *et al*., 2014). It is also possible that longer incubation times would have resulted in a higher proportion of anabolically active organisms, as our incubation duration was determined by lab-based experiments using the more active upper sediment horizons (0–5 cm; see Experimental procedures).

In the 60.7 mm horizon, quartz grains had the lowest cell abundances per unit surface area and volume of the three examined sections, while orthoclase and plagioclase had higher-than-average biomass densities (Table 2). The proportion of anabolically active organisms, however, was not substantially different among distinct mineral types, suggesting that cells adhere more strongly to plagioclase and orthoclase grains, and/or that quartz is more readily degraded during weathering and burial, disrupting surficial microbial association. This horizon also exhibited the highest proportion of cells located inside mineral grains (37.8%), an observation that could reflect the extensive remineralization of external biomass with burial (Mackin and Swider, 1989).

Compiling findings across horizons

When integrating sequencing and microscopy data across all horizons, intriguing trends of anabolic activity, diversity and spatial arrangement emerged. With increasing depth into the sediment, where geochemical and thermal conditions were more stable, alpha diversity metrics

of bulk pre-extraction communities revealed a decrease in richness but increase in evenness (Fig. S6). Among the anabolically active and inactive communities, no substantial change in the number of distinct ASVs with depth was observed, but the evenness of their distribution increased down-core for the active constituents. This pattern may reflect a wider range of available niches with fewer dominant lineages below the photic zone, as organic matter is remineralized through a range of metabolic routes, making these deeper communities' emergent effects more resistant to environmental changes (Wittebolle *et al*., 2009).

Beta diversity analysis revealed a clear separation between both bulk and extracted communities as well as between active and inactive communities (Fig. S7). The distinction between the bulk, sediment-associated community and the extractable microbes (Fig. S7A) reveals an opportunity for improved cell extraction procedures, and may be attributable to differences in DNA collection protocols, strongly adherent non-extractable cells and relic DNA not contained in cells (Carini *et al*., 2016). The community composition differences between active and inactive communities (Fig. S7B) confirms that organisms respond to environmental cues in a taxonomically differentiated manner and that anabolic activity is not a random process. Furthermore, for both active and inactive communities, the closer two sediment horizons were in depth, the more similar their community compositions. This trend likely reflects depth-based gradients that form the energetic basis for metabolic activity, as well as the
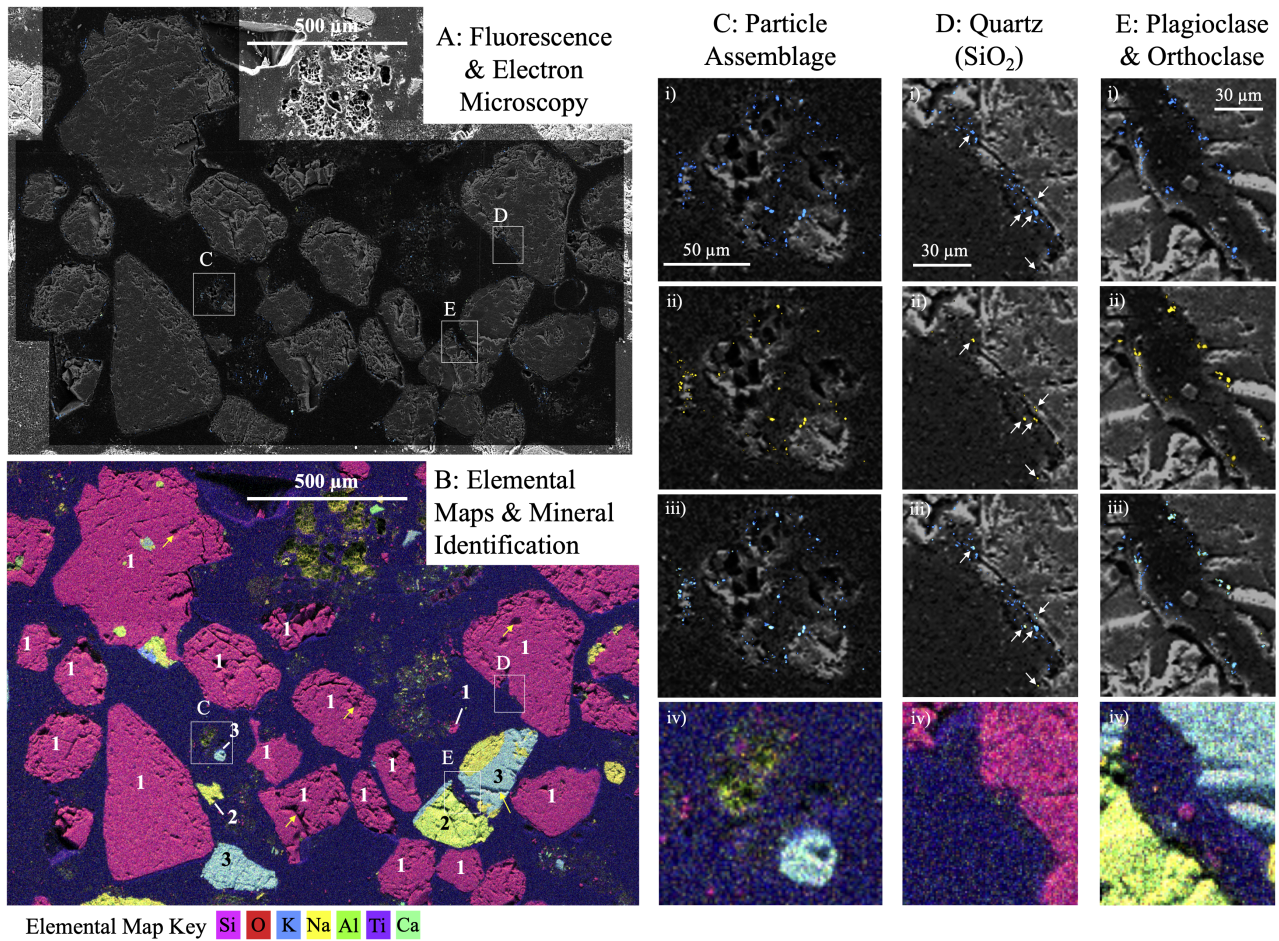
Fig. 4. Correlative fluorescence and electron microscopy from the sediment section at 12 mm sediment depth).
A. Overlain on the base SEM image are two fluorescence channels showing SYBR-active features in blue, and BONCAT-active features in yellow. The dark zonation indicates the fluorescence microscopy footprint.
B. Composite elemental maps derived from EDS analysis show the mineral grains that were analysed, labelled by mineral type. 1 = Quartz; 2 = Plagioclase; 3 = Orthoclase. Yellow arrows indicate particularly large mineral grain pore spaces for illustrative purposes. C–E show three mineralogically distinct sites in detail. (i) SYBR green, (ii) BONCAT and (iii) merged channels, as well as (iv) EDS elemental abundance maps (in which dark blue background represents the resin). In (D), zones containing BONCAT-positive biomass in (i), (ii) and (iii) are marked with white arrows. Brightness and contrast of all fluorescence microscopy views have been increased by 40% to enhance signal visibility; original images as presented in the methods can be found at the following Dropbox link: tinyurl.com/4mcw39xu [Color figure can be viewed at wileyonlinelibrary.com]

burial process in which a given horizon's community represents the confluence of local selective pressures operating on an assemblage of organisms 'imported' from above or from below due to tidal pumping.

At each of the three horizons examined through correlative microscopy, cells appeared to be distributed not as evenly spaced individual cells, but rather as aggregations suggestive of inter-organism interactions consistent with a 'sphere of influence' on the order of a few microns (Dal Co *et al*., 2020; Steinberg *et al*., 2021) (Figs 3–5). Throughout the sediment column, quartz was the dominant mineral type, yet microbial communities associated with quartz grains had the lowest proportion of anabolically active members. Other mineral types – such

as orthoclase, plagioclase and rutile – had a broader set of cations (Al, Ti, K) that may have offered additional electron transfer or nutrient acquisition opportunities for active cells. With increasing sediment depth, organisms were more likely to be located inside mineral grains, and these 'internal' cells were increasingly likely to be anabolically active compared with their 'external' counterparts (Table 2): at 7.6, 12 and 60.7 mm depth, internal organisms were 2.1%, 24% and 45% more likely to be active than those outside minerals, respectively. These observations are consistent with a more stable intra-mineral environment that may be less susceptible to predation, particularly in the more energetically constrained anoxic sediment horizons.
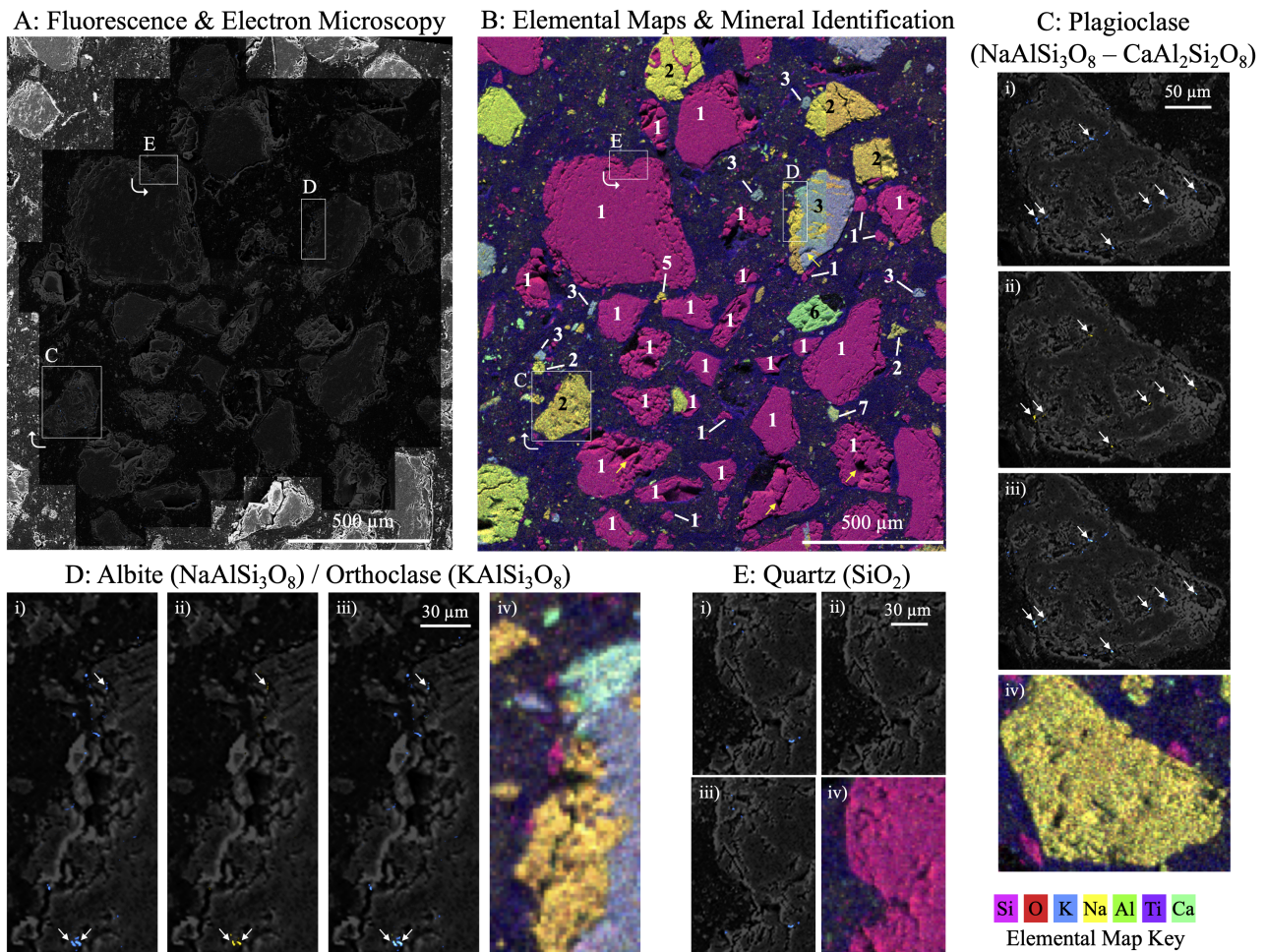
Fig. 5. Correlative fluorescence and electron microscopy from the sediment section at 60.7 mm sediment depth.
A. Overlain on the base SEM image are two fluorescence channels showing SYBR-active features in blue, and BONCAT-active features in yellow. The dark zonation indicates the fluorescence microscopy footprint.
B. Composite elemental maps derived from EDS analysis show the mineral grains that were analysed, labelled by mineral type. 1 = Quartz; 2 = Plagioclase; 3 = Orthoclase; 4 = Rutile; 5 = Albite; 6 = Ca, K, Mg, Fe silicate; 7 = Hornblende. Yellow arrows indicate particularly large mineral grain pore spaces for illustrative purposes. C–E show three mineralogically distinct sites in additional detail in (i) SYBR green, (ii) BONCAT and (iii) merged channels, as well as (iv) EDS elemental abundance maps (in which dark blue background represents the resin). In (C) and (D), zones containing BONCAT-positive biomass in (i), (ii) and (iii) are marked with white arrows. No such zones were detected in E. Brightness and contrast of all fluorescence microscopy views have been increased by 40% to enhance signal visibility; original images as presented in the methods can be found at the following Dropbox link: tinyurl.com/4mcw39xu [Color figure can be viewed at wileyonlinelibrary.com]

Conclusions

The biological community of Little Sippewissett salt marsh sediment demonstrated notable differences in its composition, anabolic activity patterns, spatial arrangements and mineralogical associations at the three distinct horizons analysed in this study. Following incorporation of HPG into new biomass during a 3.7-day *in situ* incubation experiment, correlative microscopy, BONCAT-FACS and 16S rRNA gene amplicon sequencing demonstrated that the most prevalent active constituents shifted from sulfur cycling phototrophic consortia in the surficial horizon, to putative sulfate-reducing bacteria likely oxidizing a range of organic compounds, to a range of fermentative lineages in the lower horizons. We observed a rapid decay in the proportion of active organisms from ∼60% in the top centimetre to between 9.4%–22.4% in the horizons between 2–10 cm depth, offering a quantifiable reflection of the shift to the dark, anoxic environment. By embedding sediment cores in resin, we mapped biomass and mineral grains with microscale resolution and found that, on average, organisms were most likely to be found inside mineral grains in the lowermost horizon. Plagioclase, orthoclase and rutile minerals recruited more abundant communities that contained a higher proportion of anabolically active organisms compared with quartz grains. Taken together, these findings give the

impression of a more spatially and metabolically expansive community in surface sediments, fuelled by sunlight and a range of available niches, that is streamlined by burial and mineralogical weathering.

This benchmark study presents a promising new approach for exploring the anabolic activity of a complex microbial community by mapping the precise spatial configuration of anabolically active organisms within mineralogically heterogeneous salt marsh sediment through correlative fluorescence and electron microscopy, while simultaneously identifying active organisms in neighbouring sediment with BONCAT-FACS and 16S rRNA gene sequencing. The structure, activity and evolutionary trajectory of complex microbial communities are determined by the interactions between biotic and abiotic components of an ecosystem. Spatial relationships are a powerful indication of these interactions, particularly in concert with the identification of metabolically active organisms. Looking forward, the incorporation of rRNA-targeted FISH into this workflow would enable a more direct connection between microbe-mineral spatial arrangements and taxonomically constrained activity patterns. Improved approaches for understanding microscale ecosystems in a new light, such as those presented here, reveal environmental parameters that promote or constrain metabolic activity and clarify the impact that microbial communities have on our world.

Experimental procedures

Incubation chamber construction

Customized chambers were constructed to enable *in situ* incubation with HPG-infused fluid (Fig. 1, panels 1 and 2). Glycol-modified polyethylene terephthalate (PETG) tubes (2.54 cm outer diameter, 1.91 cm inner diameter, McMaster-Carr, Elmhurst, IL) were cut to ∼30 cm length. PETG was used because of its low gas permeability and high optical transparency (Thermo Fisher Scientific), properties that diminished oxygen penetration of subsurface sediments during recovery and transport while retaining light availability for surface-exposed organisms – many of which are phototrophs – during the incubation period. The lower opening of each tube was bevelled with sandpaper (giving the tube a sharp interior edge) to minimize the effects of compaction on collected material when pressing the tube into the sediment.

To make the chambers water-tight, the top portions of two 50-ml Falcon tubes were cut off and attached to either end of the PETG tube using Master Plumber epoxy putty (William H. Harvey, Omaha, NE). By threading the lids onto the appended tube tops, fluid was retained within the incubation tube; by removing them, percolation was enabled.

At certain times during the incubation, gas-permeable, liquid-impermeable conditions were required. This was achieved with 0.25 mm-thick silicone polydimethylsiloxane (PDMS) membranes (Interstate Specialty Products, Sutton, MA) that were secured between the end of the tube and the screw-top lid. Holes were poked into the Falcon tube lid with a needle to facilitate gas exchange at both the top and bottom of the incubation volume. All materials were thoroughly cleaned with 70% ethanol and 60 min of UV light exposure prior to use.

Sample recovery, HPG addition and *in situ* incubation

On September 26, 2018, customized incubation chamber tubes were taken to Little Sippewissett salt marsh in Falmouth, MA. The 'Berry Pool' at 41.5758° latitude, −70.6394° longitude (Fig. S4) was selected for sampling due to its extensive heritage in environmental microbiology research, which would provide greater context to our studies. The work presented here pertains to sediment cores collected with six customized incubation tubes (see Table S1). Cores BM and BS were treated with HPG for BONCAT analysis; CM and CS were control samples with no HPG exposure, a treatment that avoids stimulatory effects of a methionine-enhanced control (Hatzenpichler *et al*., 2014, 2020). BM and CM were used for microscopy analysis; BS and CS were used for community analysis by FACS and subsequent 16S rRNA gene sequencing of anabolically active and inactive populations. A control of homogenized 0–10 cm depth sediment (core AM) was autoclave-sterilized and then incubated with HPG solution (described below) for 89 h in the lab. Core MM was not incubated *in situ* and was used only for fluid flow tests.

At approximately 07:00 (24-h clock), the tubes were pressed into the sediment, collecting ∼10–12 cm of sediment as well as the full overlying water column (∼15 cm); upon removal, a ∼2 cm thick autoclave-sterilized plug of glass wool (Fisher Scientific) was inserted into the bottom of the tube. (See Fig. 1 for a schematic of the collection and sample processing approach.) Permeable and intact Falcon tube caps were twisted onto the top and bottom of the chamber respectively. At approximately 7:30, the incubation chambers were placed in an anoxic glove box (3.5% H_2, 20% CO_2, 76.5% N_2), the caps were removed, and fluid replacement began. (Chambers were transported to and from the lab in a dark cooler to minimize the introduction of light to subsurface horizons.) Based on the permeability of the sediment and the glass wool plug, fluid moved through the sediment column at a rate of ∼0.3 ml min^{-1} cm^{-2}.

Next, the sediment water was replaced with fluid containing HPG (Click Chemistry Tools, Scottsdale, AZ) for anabolic uptake. For each sample, HPG was dissolved in

100 ml of 0.22 μm-filtered Berry Pool water for a final concentration of 50 μM. In an anoxic chamber, the solution was vigorously shaken several times to accelerate degassing and stored overnight. Four to six column volumes of HPG solution were added dropwise to the top of the column at roughly the same rate as fluid leaked out the bottom, resulting in a full replacement of permeable volume with HPG solution in a manner that did not substantially change the overlying pressure experienced by the sediment. PDMS membranes were secured to the top and bottom of the incubation chamber with the same Falcon tube caps as before, and the samples were transported back to the Berry Pool.

The appropriate concentration of HPG and dye for subsequent visualization was determined from a previous study (Hatzenpichler and Orphan, 2015) and tests using *E. coli* strain K12 exposed to 5–500 μM HPG and 0.5–50 μM dye (Fig. S8). For each treatment, *E. coli* was grown in M9 minimal medium (Table S2) to an OD_{600} of 1.0 (measured by Cole Parmer UV/Vis Spec.). The cells were pelleted, fixed in 3% PFA solution and stained with a Cy3 Picolyl Azide dye (Click Chemistry Tools) click staining solution (Table S3; Hatzenpichler and Orphan, 2015) for 60 min. Compared with its benchtop (oxic) equivalent, we found enhanced signal when the staining procedure was performed in an anoxic chamber (Fig. S9).

At the precise location of sample collection, the incubation chambers were placed back into the marsh sediment at 12:00. Immediately prior to deposition, holes were poked in the bottom caps (but not the membrane) to ensure the full length of the sediment was in gaseous equilibrium with its surroundings, but that the HPG solution remained contained. The tubes were aligned such that the water–sediment interface matched that of the sediment in the Berry Pool. The samples were left to incubate in the marsh for 89 h (retrieval time September 30, 05:00). The incubation timing was determined by experiments using the top five centimetres of salt marsh sediments which demonstrated apparent saturation of BONCAT-positive signal after 88 h (Fig. S10).

Throughout the process described above, the incubation chambers were checked for leaks. Overlying water levels were marked on the tube exterior after sample recovery, after HPG fluid introduction and upon re-introduction to the marsh; experiments only proceeded if no change in water level was observed.

Preparation of cores for microscopy

Our core preparation expanded on a protocol that was first used in the analysis of volcanic fumarole soils (Marlow *et al*., 2020). Cores BM and CM were chemically fixed, dehydrated, embedded in resin, sectioned and stained for analysis by fluorescence and electron microscopy. Four to six column volumes of fixative solution (3% paraformaldehyde in 0.22 μm-filtered Berry Pool water) were percolated through the samples to fully replace the HPG solution. An intact bottom cap was secured to the bottom of the core tube, and samples were incubated at room temperature for 4 h. A dehydration series consisting of 4–6 column volumes each of 50%, 80% and 96% ethanol (in 0.22 μm-filtered Berry Pool water) was performed.

Following dehydration, sediment samples were embedded in LR White resin (hard grade, Electron Microscopy Sciences, Hatfield, PA), which was selected for its low viscosity and minimal background signal under the wavelengths used for fluorescence microscopy. LR White has been used in a number of similar applications, including correlative microscopy of animal tissue (Hegermann *et al*., 2019), plant tissues (Bell *et al*., 2013), low diversity microbial biofilms (Knierim *et al*., 2012), carbonate microbialites (Gérard *et al*., 2013) and marine sediment (McGlynn *et al*., 2018). Four to six column volumes of 100% liquid resin were percolated through the dehydrated columns, and intact Falcon tube caps were secured on the bottom to avoid leakage. The samples were then placed in an incubation oven at 60 °C for 36 h to cure. (This thermal regime proved more successful at producing well-solidified sediment cores in initial tests than a ramp-up from 40 to 60 °C.)

The solidified sediment columns were cut transversely into ∼2 mm-thick sections with a diamond saw (Model 650, South Bay Technology, San Clemente, CA) and an ethanol-sterilized PELCO diamond wafering blade (#812–332, Ted Pella, Redding, CA) spun through ultrapure Milli-Q cooling water. Sections were submerged in a 5 μM Cy3 Picolyl Azide dye click staining solution (Hatzenpichler and Orphan, 2015). This staining incubation took place in the dark for 60 min in an anoxic chamber; when compared with its benchtop (oxic) equivalent, the chamber-based incubation generated a brighter signal in *E. coli* cultures (Fig. S9). Afterwards, they were removed from the chamber, washed three times with sterile PBS solution, incubated in 5× SYBR Green I (referred to hereafter as 'SYBR green'; Life Technologies, Thermo Fisher, Waltham, MA) in the dark at room temperature for 15 min, rinsed three times with sterile PBS, and left to air dry in the dark prior to imaging. All downstream correlative microscopy was performed on areas as far from the outer edge of the sediment core as possible (∼8 mm) in order to minimize the effects of the coring process (e.g. microscale sediment disturbance and light transmission) on the analysed area.

Fluorescence microscopy

Fluorescence imaging of sectioned samples was done with an LSM 880 confocal laser scanning microscope (Zeiss, Oberkochen, Germany) equipped with a gallium arsenide phosphide (GaAsP) detector, a 20× objective lens and DI water immersion. Argon and DPSS lasers provided excitation at 458, 488, 514 and 561 nm wavelengths. Detected emission windows were 510–561 nm for SYBR green and 564–669 nm for Cy3. Reflected light from the 488 nm laser was also captured to link sample features between confocal and electron microscopy images as reference points. Imaging was done with the Zen 2.3 SP1 program (Zeiss). Focus was adjusted manually for each field of view. 1024 × 1024 pixel frames were acquired with a pixel dwell time of 32.77 μs and a pixel size of 240 nm. Four line-based scans were averaged to generate each image. Gain settings were set to minimize background and non-specific signals. For the SYBR channel, 800 master gain and 1.3 digital gain were used; these parameters were 680 and 1.2 respectively, for the Cy3 channel.

Electron microscopy and energy dispersive X-ray spectroscopy

After fluorescence microscopy, each section was dipped in a dehydration series of 50%, 80% and 100% ethanol solutions (balance Milli-Q water). The sample was then mounted on an SEM sample holder with double-sided carbon tape, sputter-coated with 5 nm of Pt/Pd (EMS 150 T S Metal Sputter Coater, Electron Microscopy Science, Hatfield, PA), and loaded into a JEOL JSM 7900F Schottky FE-SEM. Using the Zeiss SmartSEM software, secondary electron images were collected at a voltage of 12 kV using an Everhart–Thornley detector. The voltage was increased to 20 kV for elemental analysis via an Oxford Ultim Max EDS Detector. Elemental abundances of S, Fe, K, Ca, Mg, Ti, Na, Si, Al, O and C were acquired, and data were processed with the EDAX Genesis software (Ametek, Berwyn, PA). Elemental maps were used for visualization purposes, supported by quantitative area-based scans to inform mineral identification by X-ray diffraction (XRD).

X-ray diffraction

XRD was performed using an X'Pert3 powder diffractometer by Panalytical using a Cu Kα source to scan from 5° to 70° 2θ. The sample consisted of 0–8 cm homogenized Berry Pool sediment collected on September 26, 2018 adjacent to the incubation cores, and was prepared as a packed powder by sterile mortar and pestle. The absence of internal standards precluded precise quantification of constituent mineral phases. The sample was scanned wobbling the sample stage at 0°, −1° and +1°, and the final scan (Fig. S11) was an average of these three scans. Phase identification and semi-quantitative analysis of diffractograms were performed using the HighScore Plus software by Panalytical (Malvern Panalytical, Malvern, United Kingdom).

Image processing

Fluorescence microscopy images were processed in Fiji/ImageJ version 2.0.0-rc-69/1.52p (Schindelin *et al.*, 2012). We used the DeconvolutionLab2 plugin (Sage *et al.*, 2017) with a point spread function calculated by the Zen program (based on our specific imaging parameters) and five iterations of the Richardson-Lucy algorithm (Richardson, 1972; Lucy, 1974). The Despeckle program was used for denoising.

To link the location of fluorescent signal with the high-resolution textural information enabled by electron microscopy, image co-registration was performed using the bUnwarpJ algorithm (Arganda-Carreras *et al.*, 2006) using the following parameters: accurate registration, very coarse initial deformation, super fine final deformation, 0.1 divergence weight, 0.1 curl weight, 3.5 landmark weight, 0.0 image weight, 10 consistency weight and 0.1 stop threshold. The SEM/EDS images were designated as the 'target' images onto which fluorescence images were mapped, and approximately one landmark per 10 000 μm^2 was designated on the SEM and reflected light fluorescence images. The other two fluorescence channels (SYBR green and Cy3) were anchored to the reflected light layer to accurately co-register SYBR and BONCAT signals with SEM and EDS data (see Fig. S12).

Cell counting and distance relationships were analysed in Matlab R2018b (see Supporting Information for details). Red (Cy3, BONCAT) and green (SYBR green, all cells) channels were separated and converted to binary images at a manually determined global threshold of 0.04. Single pixels were eliminated to remove noise, and individual regions of interest were designated by applying a watershed transform with four-degree connectivity (e.g. pixels that only touched at corners rather than edges were not counted as the same object). Finally, centroid holes were filled, and the remaining shapes were counted as 'organisms'. An organism was recorded as anabolically active if at least one of its pixels fluoresced both red and green after being subjected to the image analysis pipeline.

Organism concentrations were calculated by counting the number of organisms in the relevant field of view and dividing that number by the volume sampled through fluorescence microscopy. This volume was determined using the *x* and *y* dimensions of the microscopy footprint and

the *z* dimension (1.66 μm) empirically established by an average of the SYBR green and Cy3 signal transmission distances through the resin, as shown in Fig. S13.

The mineral grain with which a given organism was putatively associated was determined by measuring the distances between organisms and mineral surfaces. The outlines of mineral grains were manually traced in Adobe Photoshop using the high-resolution SEM images and then converted into a binary image in Matlab. Next, we calculated the shortest Euclidean distance from each organism's outer surface to the perimeter of each mineral. The shortest distance and identity of the associated mineral were recorded. Because this analysis was restricted to a two-dimensional cross-sectional view of three-dimensional mineral grains, distances between an organism and its nearest mineral surface must be interpreted as upper bounds. The relative placement of an organism with respect to a mineral boundary – interior or exterior – would not change based on additional three-dimensional information. To exclude cells that had been dislodged during the embedding and sectioning process, all cells more than 70 μm away from the nearest mineral surface were omitted from distance-based calculations. This cutoff, which removed 6.2% of all organisms from spatial analysis only, was based on a distance histogram to determine outliers (Fig. S14) and is within the range of biofilm thicknesses associated with silica mineral surfaces (which represented the majority of observed mineral grains) (Ye *et al.*, 2015). During sectioning, a few mineral grains were plucked from the resin: three in the top section, two in the middle and three in the bottom. Some organisms associated with these plucked grains remained in the resin but were not included in spatial analyses. The overall loss of material indicates that cell abundance values represent a lower bound, as organisms found within the plucked grains' pore spaces were not seen. When normalizing organism abundances by mineral surface area and volume, perimeters calculated from mineral grain outlines were used as a proxy for surface area, and cross-sectional area was used as a proxy for grain volume.

Fluorescence-activated cell sorting

Samples BS and CS were used for FACS and high-throughput 16S rRNA gene sequencing to identify the subset of microorganisms that were anabolically active during the incubation period. These cores were chemically fixed in 3% paraformaldehyde as described for cores BM and CM above. BS and CS were then rinsed with 4–6 column volumes of 0.22 μm-filtered Berry Pool water. Prior to shipment, the overlying liquid was removed and the top 1.0 cm (±0.3 cm) flocculent layer of sediment was transferred to a separate sterile tube to avoid compression and inaccurate identification of horizons. Sterile glass wool was added to the top of the incubation chamber to maintain core coherence during transport. Cores BS and CS were shipped on ice from Massachusetts to Montana State University for analysis (shipment took ∼19 h).

Upon arrival, each sediment core was carefully excised from the core sleeve using a custom-built, sterilized plunger. Each core was divided into 1 cm increments, which were weighed, transferred into Falcon tubes containing 10 ml of sterilized 1× PBS and stored at 4°C until cells were extracted. Cells were extracted from each sediment layer using methods adapted from Couradeau *et al.* (2019) with the following modifications. For each sediment layer, 1 ml of the slurry was diluted with 5 ml of sterile PBS in a 15 ml Falcon tube with Tween20 (final concentration 0.02%). The cell extraction slurry was placed on a benchtop vortexer at maximum speed for 5 min. Large sediment particles, and, on occasion, incompletely disaggregated pink berries, were pelleted via centrifugation at 500*g* for 55 min. Cells from 700 μl of the supernatant were pelleted in a 1.5 ml microcentrifuge tube by centrifugation at 16 000*g* for 5 min. The supernatant was carefully removed by pipette before the click reaction was performed directly on the cell pellet. Extraction blanks were performed without any added sediment in parallel with cell extractions to test for reagent contamination.

The click reaction solution was prepared in a large volume in order to stain all samples using the same solution. The reaction solution was prepared as previously described (Hatzenpichler and Orphan, 2015) with the addition of a general DNA stain, SYBR green (Thermo Fisher Scientific, Invitrogen, Eugene, OR, USA) to counterstain all cells. The solution contained 5 mM aminoguanidine hydrochloride (Sigma Aldrich), 5 mM sodium L-ascorbate (Sigma Aldrich), 100 μM copper sulfate pentahydrate (Sigma Aldrich), 500 μM THPTA (Click Chemistry Tools), 12 μM Cy5 picolyl-azide dye (Click Chemistry Tools) and 1× SYBR green in PBS. The solution was vortexed, and 200 μl was transferred to each cell pellet and mixed with cells by pipetting up and down. The click reaction solution and cells were incubated for 30 min in the dark on a slow rotator at room temperature. Click reaction solution was washed from cells by three cycles of (i) centrifugation at 17 000*g* for 5 min, (ii) removal of supernatant by pipette and (iii) resuspension in sterile PBS. The final cell pellet was resuspended in 700 μl of sterile 1× PBS. Prior to cell sorting, the cell suspension was passed through a 35 μm filter cap (BD-falcon 5 ml tube with cell strainer cap, Corning™, Corning, NY, USA) to remove any remaining large debris.

A Sony SH800S FACS (Sony Biotechnology, San Jose, CA) was used to sort cells via a 70 μm chip. The

cell sorter was set to detect the SYBR green dye on the green channel (excitation 488 nm, emission 525 ± 50 nm) and the BONCAT-associated Cy5 dye on the red channel (excitation 638 nm, emission 665 ± 30 nm). The first two gates were drawn on forward scatter and backscatter properties to remove any large particles or noise. The third gate was drawn on SYBR green positive ('sortable cells') events, with the assumption that this gate captured all cells. Only SYBR+ cells were gated to be either BONCAT positive ('active cells') or BONCAT negative ('inactive cells') on the Cy5 channel. Core CS, the no-HPG control, was used to determine the cutoff between BONCAT positive and negative fractions. The absence of a gap between the BONCAT+ and BONCAT− gates allowed us to capture all of the cells, and while the conservatively drawn gates minimized the possibility of false positives, false negatives were likely captured (Fig. S5). For each of three biological replicates for each cell fraction ('active cells' and 'inactive cells'), 1×10^6 cells were sorted into 1.5 ml microcentrifuge tubes containing 500 μl of sterile 1× PBS. Sorted cells were stored at 4 °C for up to 6 h before being centrifuged at 17 000*g* for 5 min to pellet and then resuspended in 20 μl of nuclease-free water and frozen at −80 °C until DNA extraction and downstream processing.

16S rRNA gene amplicon sequencing

To capture the bulk microbial community from each sediment layer in core BS, DNA was extracted from 500 μl sediment/1× PBS slurry from each layer using the FastDNA Spin Kit for Soils (MP Biomedicals, Irvine, CA) following the manufacturer's instructions. A blank DNA extraction was processed in parallel with bulk sediment extractions to check for contaminants. DNA was extracted from sorted cells and processing blanks as previously described (Reichart *et al*., 2020). Briefly, cell suspensions were transferred to a 96-well microtiter plate and sealed with sterile adhesive foil before being subjected to three freeze–thaw cycles (−80 °C for 20 min, 99 °C for 10 min), with brief centrifugation prior to each freezing step. 16S rRNA genes of bacteria and archaea were amplified following the Earth Microbiome protocol (Thompson *et al*., 2017) using revised primers 515F (5′-GTG**Y**CAGCMGCCGCGGTAA; Parada *et al*., 2016) and 806R (5′-GGACTACNVGGGTWTCTAAT; Apprill *et al*., 2015) added directly into the extracted DNA microtiter plates. These primers were designed prior to the discovery of several new lineages related to the DPANN and Asgard archaea superphyla (Baker *et al*., 2020) and thus do not capture the entire archaeal diversity (Bahram *et al*., 2019; Pausan *et al*., 2019). However, their extensive use in environmental microbiology laboratories around the world enables comparability between studies

(Gilbert *et al*., 2014; Thompson *et al*., 2017) and within our own laboratories. The final PCR volume was 37.5 μl and consisted of 15 μl Invitrogen Platinum Taq II 2× Master Mix, 0.75 μl 515F primer (10 μM; final: 0.2 μM), 0.75 μl 806R primer (10 μM; final: 0.2 μM) and 1 μl nuclease-free water added directly into the microtiter plates containing the 20 μl of lysate. The thermocycler conditions were 94 °C for 3 min followed by 28 cycles of 94 °C for 45 s, 50 °C for 60 s, and 72 °C for 90 s before a final elongation step at 72 °C for 10 min. A negative PCR control was processed in parallel using nuclease-free water instead of extracted DNA to check for PCR contaminants. PCR products were purified using AMPure XR beads (Beckman Coulter) following the manufacturer's protocol with a final elution in 40 μl nuclease-free water.

Afterwards, a second PCR to attach barcodes and sequencing adapters to the 16S rRNA gene amplicons was performed. The final volume of the PCR was 25 μl and contained 5 μl purified, amplified DNA, 12 μl Invitrogen Platinum Taq II 2× Master Mix, 2.5 μl i5 primer (final: 0.25 μM), 2.5 μl i7 primer (final: 0.25 μM) and 2.5 μl water. The thermocycler conditions were 95 °C for 3 min followed by 8 cycles of 95 °C for 30 s, 55 °C for 30 s, and 72 °C for 30 s, followed by a final elongation step at 72 °C for 5 min. A PCR product purification was performed as described above using AMPure XR beads. Finally, purified PCR products were checked for appropriate length by gel electrophoresis in 1% agarose. Amplicons were quantified in triplicate using Quant-iT Picogreen dsDNA Assay (Invitrogen) following the manufacturer's protocol and measured on a Biotek Synergy H1 Hybrid microplate reader. Samples were pooled at 10 ng DNA each, and the final pooled sample was purified and concentrated with the QIAquick PCR purification spin column kit (Qiagen) following the manufacturer's guidelines. Sequencing was performed by Laragen (Culver City, CA) using Illumina 2 × 250 paired-end read MiSeq sequencing. Sequences have been archived at NCBI GenBank under the Bioproject ID PRJNA643437.

Sequence analysis

Primers were removed from demultiplexed sequences using *cutadapt* (Martin, 2011) with a max mismatch of 2 bp and a requirement that primers must be present on both forward and reverse reads to maintain the read pair in the dataset. Unpaired primer-free reads were processed in *DADA2* (Callahan *et al*., 2016) run in the R environment. Reads were first trimmed to 220 bp for forward reads and 170 bp for reverse reads, then were filtered with default settings of maxN = 0, maxEE = c(2,2), trunc = 2 and rm.phix = TRUE. Denoising of reads was conducted with *DADA2*'s error model calculated on randomly sampled reads from the entire dataset. Forward

and reverse reads were merged with a 20 bp minimum overlap and no mismatches. Chimaeras were removed within *DADA2* using the 'consensus' method. Taxonomy of the ASVs was assigned using *DADA2*'s built-in native implementation of a naïve Bayesian classifier (Wang *et al*., 2007) with a trained SILVA132 database (Quast *et al*., 2012). To remove contaminating sequences, R package *decontam* (Davis *et al*., 2018) was implemented using the 'prevalence' model with a threshold of 0.7, which removed 150 of the total 11 014 619 ASVs. Five samples with fewer than 10 000 sequences were removed from the dataset. Further normalization of read count per sample was performed using the R package *metagenomeSeq* (Paulson *et al*., 2013). *metagenomeSeq* builds a statistical model to account for undersampling, which was an appropriate adjustment given the high cell abundance and high anticipated diversity in Sippewissett sediments. Diversity metrics including Shannon's diversity index, Bray–Curtis similarity and non-metric multidimensional scaling were calculated in the *Phyloseq* (McMurdie and Holmes, 2013) R package.

The primers used in this study can amplify some eukaryotic sequences (Parada *et al*., 2016), but the short sequence length precludes accurate taxonomic assignment to eukaryotic chloroplast or mitochondria. While these constituents were present in 'bulk' community assessments at most horizons, they were seemingly selected against during the cell extraction and sorting process, as their relative abundance in the active and inactive fractions were all well below 1%. Mitochondrial ASVs accounted for 0.12% and 0.01% of sequences in active and inactive fractions respectively; chloroplast ASVs were 0% and 0.01% respectively.

Acknowledgements

References

Abdul-Aziz, O.I., Ishtiaq, K.S., Tang, J., Moseman-Valtierra, S., Kroeger, K.D., Gonneea, M.E., *et al*. (2018) Environmental controls, emergent scaling, and predictions of greenhouse gas (GHG) fluxes in coastal salt marshes. *J Geophys Res Biogeo* **123**: 2234–2256.

Andersen, S.B., Marvig, R.L., Molin, S., Krogh Johansen, H., and Griffin, A.S. (2015) Long-term social dynamics drive loss of function in pathogenic bacteria. *Proc Natl Acad Sci U S A* **112**: 10756.

Apprill, A., McNally, S., Parsons, R., and Weber, L. (2015) Minor revision to V4 region SSU rRNA 806R gene primer greatly increases detection of SAR11 bacterioplankton. *Aquat Microb Ecol* **75**: 129–137.

Arganda-Carreras, I., Sorzano, C.O., Marabini, R., Carazo, J.M., Ortiz-de-Solorzano, C., and Kybic, J. (2006) Consistent and elastic registration of histological sections using vector-spline regularization. In *International Workshop on Computer Vision Approaches to Medical Image Analysis* (pp. 85–95). Heidelberg, Berlin: Springer.

Bagert, J.D., Xie, Y.J., Sweredoski, M.J., Qi, Y., Hess, S., Schuman, E.M., and Tirrell, D.A. (2014) Quantitative, time-resolved proteomic analysis by combining bioorthogonal noncanonical amino acid tagging and pulsed stable isotope labeling by amino acids in cell culture. *Mol Cell Proteomics* **13**: 1352–1358.

Bahr, M., Crump, B.C., Klepac-Ceraj, V., Teske, A., Sogin, M.L., and Hobbie, J.E. (2005) Molecular characterization of sulfate-reducing bacteria in a New England salt marsh. *Environ Microbiol* **7**: 1175–1185.

Bahram, M., Anslan, S., Hildebrand, F., Bork, P., and Tedersoo, L. (2019) Newly designed 16S rRNA metabarcoding primers amplify diverse and novel archaeal taxa from the environment. *Environ Microbiol Rep* **11**: 487–494.

Baker, B.J., De Anda, V., Seitz, K.W., Dombrowski, N., Santoro, A.E., and Lloyd, K.G. (2020) Diversity, ecology and evolution of archaea. *Nat Microbiol* **5**: 887–900.

Bang-Andreasen, T., Schostag, M., Priemé, A., Elberling, B., and Jacobsen, C.S. (2017) Potential microbial contamination during sampling of permafrost soil assessed by tracers. *Sci Rep* **7**: 1–11.

Bell, K., Mitchell, S., Paultre, D., Posch, M., and Oparka, K. (2013) Correlative imaging of fluorescent proteins in resin-embedded plant material1. *Plant Physiol* **161**: 1595–1603.

Blume, E., Bischoff, M., Reichert, J., Moorman, T., Konopka, A., and Turco, R. (2002) Surface and subsurface microbial biomass, community structure and metabolic activity as a function of soil depth and season. *Appl Soil Ecol* **20**: 171–181.

Boetius, A., Ravenschlag, K., Schubert, C.J., Rickert, D., Widdel, F., Gieseke, A., *et al*. (2000) A marine microbial consortium apparently mediating anaerobic oxidation of methane. *Nature* **407**: 623.

Boldareva, E., Moskalenko, A., Makhneva, Z., Tourova, T., Kolganova, T., and Gorlenko, V. (2009) Rubribacterium polymorphum gen. nov., sp. nov., a novel alkaliphilic nonsulfur purple bacterium from an eastern Siberian soda lake. *Microbiology* **78**: 732–740.

Bowen, J.L., Morrison, H.G., Hobbie, J.E., and Sogin, M.L. (2012) Salt marsh sediment diversity: a test of the variability of the rare biosphere among environmental replicates. *ISME J* **6**: 2014–2023.

Buckley, D.H., Baumgartner, L.K., and Visscher, P.T. (2008) Vertical distribution of methane metabolism in microbial

mats of the great Sippewissett salt marsh. *Environ Microbiol* **10**: 967–977.

Callahan, B.J., McMurdie, P.J., Rosen, M.J., Han, A.W., Johnson, A.J.A., and Holmes, S.P. (2016) DADA2: high-resolution sample inference from Illumina amplicon data. *Nat Methods* **13**: 581.

Carini, P., Marsden, P.J., Leff, J.W., Morgan, E.E., Strickland, M.S., and Fierer, N. (2016) Relic DNA is abundant in soil and obscures estimates of soil microbial diversity. *Nat Microbiol* **2**: 16242.

Cordero, O.X., and Datta, M.S. (2016) Microbial interactions and community assembly at microscales. *Curr Opin Microbiol* **31**: 227–234.

Cordero, O.X., Ventouras, L.-A., DeLong, E.F., and Polz, M. F. (2012) Public good dynamics drive evolution of iron acquisition strategies in natural bacterioplankton populations. *Proc Natl Acad Sci U S A* **109**: 20059–20064.

Couradeau, E., Sasse, J., Goudeau, D., Nath, N., Hazen, T. C., Bowen, B.P., *et al*. (2019) Probing the active fraction of soil microbiomes using BONCAT-FACS. *Nat Commun* **10**: 2770.

Coyte, K.Z., Schluter, J., and Foster, K.R. (2015) The ecology of the microbiome: networks, competition, and stability. *Science* **350**: 663.

Curtis, C. (1987) Mineralogical consequences of organic matter degradation in sediments: inorganic/organic diagenesis. In *Marine Clastic Sedimentology*: Dordrecht: Springer, pp. 108–123.

Dal Co, A., van Vliet, S., Kiviet, D.J., Schlegel, S., and Ackermann, M. (2020) Short-range interactions govern the dynamics and functions of microbial communities. *Nat Ecol Evol* **4**: 366–375.

Daly, R.A., Wrighton, K.C., and Wilkins, M.J. (2018) Characterizing the deep terrestrial subsurface microbiome. In *Microbiome Analysis*: New York, NY: Springer, pp. 1–15.

Dang, H., Li, T., Chen, M., and Huang, G. (2008) Cross-ocean distribution of Rhodobacterales bacteria as primary surface colonizers in temperate coastal marine waters. *Appl Environ Microbiol* **74**: 52–60.

Davis, N.M., Proctor, D.M., Holmes, S.P., Relman, D.A., and Callahan, B.J. (2018) Simple statistical identification and removal of contaminant sequences in marker-gene and metagenomics data. *Microbiome* **6**: 226.

Dieterich, D.C., Link, A.J., Graumann, J., Tirrell, D.A., and Schuman, E.M. (2006) Selective identification of newly synthesized proteins in mammalian cells using bioorthogonal noncanonical amino acid tagging (BONCAT). *Proc Natl Acad Sci U S A* **103**: 9482–9487.

Dong, H., Jaisi, D.P., Kim, J., and Zhang, G. (2009) Microbe-clay mineral interactions. *Am Mineral* **94**: 1505–1519.

Ford, T.E. (1993) Aquatic microbiology, an ecological approach. Cambridge, Mass: Backwell Scientific Publication. Inc. pp. 239–250.

Fierer, N., Bradford, M.A., and Jackson, R.B. (2007) Toward an ecological classification of soil bacteria. *Ecology* **88**: 1354–1364.

Gandy, E.L., and Yoch, D.C. (1988) Relationship between nitrogen-fixing sulfate reducers and fermenters in salt marsh sediments and roots of *Spartina alterniflora*. *Appl Environ Microbiol* **54**: 2031.

Gérard, E., Ménez, B., Couradeau, E., Moreira, D., Benzerara, K., Tavera, R., and López-García, P. (2013) Specific carbonate–microbe interactions in the modern microbialites of Lake Alchichica (Mexico). *ISME J* **7**: 1997–2009.

Gilbert, J.A., Jansson, J.K., and Knight, R. (2014) The earth microbiome project: successes and aspirations. *BMC Biol* **12**: 69.

Goeppert, N., and Goldscheider, N. (2011) Transport and variability of fecal bacteria in carbonate conglomerate aquifers. *Groundwater* **49**: 77–84.

Gómez-Pereira, P.R., Schüler, M., Fuchs, B.M., Bennke, C., Teeling, H., Waldmann, J., *et al*. (2012) Genomic content of uncultured Bacteroidetes from contrasting oceanic provinces in the North Atlantic Ocean. *Environ Microbiol* **14**: 52–66.

Gong, B., Wu, P., Ruan, B., Zhang, Y., Lai, X., Yu, L., *et al*. (2018) Differential regulation of phenanthrene biodegradation process by kaolinite and quartz and the underlying mechanism. *J Hazard Mater* **349**: 51–59.

Gyngard, F., and Steinhauser, M.L. (2019) Biological explorations with nanoscale secondary ion mass spectrometry. *J Anal At Spectrom* **34**: 1534–1545.

Hapca, S., Baveye, P.C., Wilson, C., Lark, R.M., and Otten, W. (2015) Three-dimensional mapping of soil chemical characteristics at micrometric scale by combining 2D SEM-EDX data and 3D X-ray CT images. *PLoS One* **10**: e0137205.

Hatzenpichler, R., Connon, S.A., Goudeau, D., Malmstrom, R.R., Woyke, T., and Orphan, V.J. (2016) Visualizing in situ translational activity for identifying and sorting slow-growing archaeal–bacterial consortia. *Proc Natl Acad Sci U S A* **113**: E4069–E4078.

Hatzenpichler, R., Krukenberg, V., Spietz, R.L., and Jay, Z.J. (2020) Next-generation physiology approaches to study microbiome function at single cell level. *Nat Rev Microbiol* **18**: 241–256.

Hatzenpichler, R., and Orphan, V.J. (2015) Detection of protein-synthesizing microorganisms in the environment via bioorthogonal noncanonical amino acid tagging (BONCAT). In T.J McGenity, (ed.), *Hydrocarbon and Lipid Microbiology Protocols*. Berlin, Heidelberg: Springer. pp. 145–157.

Hatzenpichler, R., Scheller, S., Tavormina, P.L., Babin, B.M., Tirrell, D.A., and Orphan, V.J. (2014) In situ visualization of newly synthesized proteins in environmental microbes using amino acid tagging and click chemistry. *Environ Microbiol* **16**: 2568–2590.

Hegermann, J., Wrede, C., Fassbender, S., Schliep, R., Ochs, M., Knudsen, L., and Mühlfeld, C. (2019) Volume-CLEM: a method for correlative light and electron microscopy in three dimensions. *Am J Physiol-Lung Cell Mol Physiol* **317**: L778–L784.

Hell, R., Dahl, C., Knaff, D.B., and Leustek, T. (2008) *Sulfur Metabolism in Phototrophic Organisms* (Vol. 27). Springer Science & Business Media.

Hester, E.R., Harpenslager, S.F., van Diggelen, J.M., Lamers, L.L., Jetten, M.S., Lüke, C., *et al*. (2018) Linking nitrogen load to the structure and function of wetland soil and rhizosphere microbial communities. *mSystems* **3**: e00214-17.

Hinz, F.I., Dieterich, D.C., Tirrell, D.A., and Schuman, E.M. (2011) Noncanonical amino acid labeling in vivo to visualize and affinity purify newly synthesized proteins in larval zebrafish. *ACS Chem Nerosci* **3**: 40–49.

House, C.H., Cragg, B.A., and Teske, A. (2003) Drilling contamination tests during ODP leg 201 using chemical and particulate tracers. In *Proceedings of the Ocean Drilling Program*, Initial Reports.

Howarth, R.W., and Giblin, A. (1983) Sulfate reduction in the salt marshes at Sapelo Island, Georgia 1. *Limnol Oceanogr* **28**: 70–82.

Howarth, R.W., and Merkel, S. (1984) Pyrite formation and the measurement of sulfate reduction in salt marsh sediments 1. *Limnol Oceanogr* **29**: 598–608.

Howarth, R.W., and Teal, J.M. (1979) Sulfate reduction in a New England salt marsh 1. *Limnol Oceanogr* **24**: 999–1013.

Hunter, C.N., Daldal, F., Thurnauer, M.C., and Beatty, J.T. (2009) *The purple phototrophic bacteria* (Vol. **28**, p. 549). Dordrecht, The Netherlands: Springer.

Jochum, L.M., Schreiber, L., Marshall, I.P., Jørgensen, B.B., Schramm, A., and Kjeldsen, K.U. (2018) Single-cell genomics reveals a diverse metabolic potential of uncultivated Desulfatiglans-related Deltaproteobacteria widely distributed in marine sediment. *Front Microbiol* **9**: 2038.

Jörgensen, R.G., Raubuch, M., and Brandt, M. (2002) Soil microbial properties down the profile of a black earth burie by colluvium. *J Plant Nutr Soil Sci* **165**: 274–280.

Kawano, M., and Tomita, K. (2002) Microbiotic formation of silicate minerals in the weathering environment of a pyroclastic deposit. *Clays Clay Miner* **50**: 99–110.

Knierim, B., Luef, B., Wilmes, P., Webb, R.I., Auer, M., Comolli, L.R., and Banfield, J.F. (2012) Correlative microscopy for phylogenetic and ultrastructural characterization of microbial communities. *Environ Microbiol Rep* **4**: 36–41.

Kostka, J.E., Roychoudhury, A., and Van Cappellen, P. (2002) Rates and controls of anaerobic microbial respiration across spatial and temporal gradients in saltmarsh sediments. *Biogeochemistry* **60**: 49–76.

Labonté, J.M., Lever, M.A., Edwards, K.J., and Orcutt, B.N. (2017) Influence of igneous basement on deep sediment microbial diversity on the eastern Juan de Fuca Ridge flank. *Front Microbiol* **8**: 1434.

LaRowe, D., Arndt, S., Bradley, J., Estes, E., Hoarfrost, A., Lang, S., *et al*. (2020) The fate of organic carbon in marine sediments-new insights from recent data and analysis. *Earth-Sci Rev* **204**: 103146.

Larsen, S., Nielsen, L.P., and Schramm, A. (2015) Cable bacteria associated with long-distance electron transport in New England salt marsh sediment. *Environ Microbiol Rep* **7**: 175–179.

Lehner, F., Kudlinzki, D., Richter, C., Müller-Werkmeister, H. M., Eberl, K.B., Bredenbeck, J., *et al*. (2017) Impact of azidohomoalanine incorporation on protein structure and ligand binding. *Chembiochem* **18**: 2340–2350.

Leizeaga, A., Estrany, M., Forn, I., and Sebastián, M. (2017) Using click-chemistry for visualizing in situ changes of translational activity in planktonic marine bacteria. *Front Microbiol* **8**: 2360.

Lovley, D.R., and Phillips, E.J. (1988) Novel mode of microbial energy metabolism: organic carbon oxidation coupled to dissimilatory reduction of iron or manganese. *Appl Environ Microbiol* **54**: 1472–1480.

Lozupone, C.A., and Knight, R. (2007) Global patterns in bacterial diversity. *Proc Natl Acad Sci U S A* **104**: 11436–11440.

Lu, A., Li, Y., Jin, S., Wang, X., Wu, X.-L., Zeng, C., *et al*. (2012) Growth of non-phototrophic microorganisms using solar energy through mineral photocatalysis. *Nat Commun* **3**: 1–8.

Lucy, L.B. (1974) An iterative technique for the rectification of observed distributions. *Astron J* **79**: 745.

Mackey, K.R., Hunter-Cevera, K., Britten, G.L., Murphy, L. G., Sogin, M.L., and Huber, J.A. (2017) Seasonal succession and spatial patterns of Synechococcus microdiversity in a salt marsh estuary revealed through 16S rRNA gene oligotyping. *Front Microbiol* **8**: 1496.

Mackin, J.E., and Swider, K.T. (1989) Organic matter decomposition pathways and oxygen consumption in coastal marine sediments. *J Mar Res* **47**: 681–716.

Marlow, J.J., Colocci, I., Jungbluth, S.P., Weber, N.M., Gartman, A., and Kallmeyer, J. (2020) Mapping metabolic activity at single cell resolution in intact volcanic fumarole sediment. *FEMS Microbiol Lett* **367**: fnaa031.

Martin, M. (2011) Cutadapt removes adapter sequences from high-throughput sequencing reads. *EMBnet J* **17**: 10–12.

McGlynn, S.E., Chadwick, G.L., Kempes, C.P., and Orphan, V.J. (2015) Single cell activity reveals direct electron transfer in methanotrophic consortia. *Nature* **526**: 531.

McGlynn, S.E., Chadwick, G.L., O'Neill, A., Mackey, M., Thor, A., Deerinck, T.J., *et al*. (2018) Subgroup characteristics of marine methane-oxidizing ANME-2 archaea and their syntrophic partners as revealed by integrated multimodal analytical microscopy. *Appl Environ Microbiol* **84**: e00399-18.

McMurdie, P.J., and Holmes, S. (2013) phyloseq: an R package for reproducible interactive analysis and graphics of microbiome census data. *PLoS One* **8**: e61217.

Mead, G. (1971) The amino acid-fermenting clostridia. *Microbiology* **67**: 47–56.

Mills, A.L., Herman, J.S., Hornberger, G.M., and DeJesús, T. H. (1994) Effect of solution ionic strength and iron coatings on mineral grains on the sorption of bacterial cells to quartz sand. *Appl Environ Microbiol* **60**: 3300–3306.

Mitri, S., Clarke, E., and Foster, K.R. (2016) Resource limitation drives spatial organization in microbial groups. *ISME J* **10**: 1471.

Morton, J.T., Sanders, J., Quinn, R.A., McDonald, D., Gonzalez, A., Vázquez-Baeza, Y., *et al*. (2017) Balance trees reveal microbial niche differentiation. *mSystems* **2**: e00162-16.

Musat, N., Musat, F., Weber, P.K., and Pett-Ridge, J. (2016) Tracking microbial interactions with NanoSIMS. *Curr Opin Biotechnol* **41**: 114–121.

Myers, C.R., and Nealson, K.H. (1988) Bacterial manganese reduction and growth with manganese oxide as the sole electron acceptor. *Science* **240**: 1319–1321.

O'Brien, W., and Ljungdahl, L.G. (1972) Fermentation of fructose and synthesis of acetate from carbon dioxide by Clostridium formicoaceticum. *J Bacteriol* **109**: 626–632.

Oremland, R.S., and Polcin, S. (1982) Methanogenesis and sulfate reduction: competitive and noncompetitive substrates in estuarine sediments. *Appl Environ Microbiol* **44**: 1270–1276.

Parada, A.E., Needham, D.M., and Fuhrman, J.A. (2016) Every base matters: assessing small subunit rRNA primers for marine microbiomes with mock communities, time series and global field samples. *Environ Microbiol* **18**: 1403–1414.

Pasulka, A.L., Thamatrakoln, K., Kopf, S.H., Guan, Y., Poulos, B., Moradian, A., et al. (2018) Interrogating marine virus-host interactions and elemental transfer with BONCAT and nanoSIMS-based methods. *Environ Microbiol* **20**: 671–692.

Paulson, J.N., Pop, M., and Bravo, H.C. (2013) metagenomeSeq: statistical analysis for sparse high-throughput sequencing. *Bioconductor package* **1**: 191.

Pausan, M.R., Csorba, C., Singer, G., Till, H., Schöpf, V., Santigli, E., et al. (2019) Exploring the archaeome: detection of archaeal signatures in the human body. *Front Microbiol* **10**: 2796.

Pohlner, M., Dlugosch, L., Wemheuer, B., Mills, H., Engelen, B., and Reese, B.K. (2019) The majority of active Rhodobacteraceae in marine sediments belong to uncultured genera: a molecular approach to link their distribution to environmental conditions. *Front Microbiol* **10**: 659.

Pujalte, M.J., Lucena, T., Ruvira, M.A., Arahal, D.R., and Macián, M.C. (2014) *The Family Rhodobacteraceae.* Berlin: Springer.

Quast, C., Pruesse, E., Yilmaz, P., Gerken, J., Schweer, T., Yarza, P., et al. (2012) The SILVA ribosomal RNA gene database project: improved data processing and web-based tools. *Nucleic Acids Res* **41**: D590–D596.

Reichart, N., Jay, Z.J., Krukenberg, V., Parker, A.E., Spietz, R.L., and Hatzenpichler, R. (2020) Activity-based cell sorting reveals responses of uncultured archaea and bacteria to substrate amendment. *ISME J* **14**: 2851–2861.

Richardson, W.H. (1972) Bayesian-based iterative method of image restoration. *JOSA* **62**: 55–59.

Rogers, J.R., and Bennett, P.C. (2004) Mineral stimulation of subsurface microorganisms: release of limiting nutrients from silicates. *Chem Geol* **203**: 91–108.

Romine, M.F., Rodionov, D.A., Maezato, Y., Osterman, A.L., and Nelson, W.C. (2017) Underlying mechanisms for syntrophic metabolism of essential enzyme cofactors in microbial communities. *ISME J* **11**: 1434.

Sage, D., Donati, L., Soulez, F., Fortun, D., Schmit, G., Seitz, A., et al. (2017) DeconvolutionLab2: an open-source software for deconvolution microscopy. *Methods* **115**: 28–41.

Salman, V., Yang, T., Berben, T., Klein, F., Angert, E., and Teske, A. (2015) Calcite-accumulating large sulfur bacteria of the genus Achromatium in Sippewissett Salt Marsh. *ISME J* **9**: 2503–2514.

Samo, T.J., Smriga, S., Malfatti, F., Sherwood, B.P., and Azam, F. (2014) Broad distribution and high proportion of protein synthesis active marine bacteria revealed by click chemistry at the single cell level. *Front Mar Sci* **1**: 48.

Schindelin, J., Arganda-Carreras, I., Frise, E., Kaynig, V., Longair, M., Pietzsch, T., et al. (2012) Fiji: an open-source platform for biological-image analysis. *Nat Methods* **9**: 676–682.

Schlesner, H., Rensmann, C., Tindall, B.J., Gade, D., Rabus, R., Pfeiffer, S., and Hirsch, P. (2004) Taxonomic heterogeneity within the Planctomycetales as derived by DNA–DNA hybridization, description of Rhodopirellula baltica gen. nov., sp. nov., transfer of Pirellula marina to the genus Blastopirellula gen. nov. as Blastopirellula marina comb. nov. and emended description of the genus Pirellula. *Int J Syst Evol Microbiol* **54**: 1567–1580.

Schlüter, S., Eickhorst, T., and Mueller, C.W. (2018) Correlative imaging reveals holistic view of soil microenvironments. *Environ Sci Technol* **53**: 829–837.

Sebastián, M., Estrany, M., Ruiz-González, C., Forn, I., Sala, M.M., Gasol, J.M., and Marrasé, C. (2019) High growth potential of long-term starved deep ocean opportunistic heterotrophic bacteria. *Front Microbiol* **10**: 760.

Seitz, A.P., Nielsen, T.H., and Overmann, J. (1993) Physiology of purple sulfur bacteria forming macroscopic aggregates in Great Sippewissett Salt Marsh, Massachusetts. *FEMS Microbiol Ecol* **12**: 225–235.

Shapiro, O.H., Hatzenpichler, R., Buckley, D.H., Zinder, S.H., and Orphan, V.J. (2011) Multicellular photo-magnetotactic bacteria. *Environ Microbiol Rep* **3**: 233–238.

Sharma, K., Palatinszky, M., Nikolov, G., Berry, D., and Shank, E.A. (2020) Transparent soil microcosms for live-cell imaging and non-destructive stable isotope probing of soil microorganisms. *eLife* **9**: e56275.

Shelobolina, E., Xu, H., Konishi, H., Kukkadapu, R., Wu, T., Blöthe, M., and Roden, E. (2012) Microbial lithotrophic oxidation of structural Fe (II) in biotite. *Appl Environ Microbiol* **78**: 5746–5752.

Shi, L., Dong, H., Reguera, G., Beyenal, H., Lu, A., Liu, J., et al. (2016) Extracellular electron transfer mechanisms between microorganisms and minerals. *Nat Rev Microbiol* **14**: 651.

Sletten, E.M., and Bertozzi, C.R. (2009) Bioorthogonal chemistry: fishing for selectivity in a sea of functionality. *Angew Chem Int Ed* **48**: 6974–6998.

Smith, D.C., Spivack, A.J., Fisk, M.R., Haveman, S.A., Staudigel, H., and Party, L. (2000) Methods for quantifying potential microbial contamination during deep ocean coring. *Ocean Drilling Program Technical Note*.

Soetaert, K., Hofmann, A.F., Middelburg, J.J., Meysman, F.J., and Greenwood, J. (2007) Reprint of "The effect of biogeochemical processes on pH". *Mar Chem* **106**: 380–401.

Spain, A.M., Krumholz, L.R., and Elshahed, M.S. (2009) Abundance, composition, diversity and novelty of soil Proteobacteria. *ISME J* **3**: 992–1000.

Spring, S., Fiebig, A., Riedel, T., Göker, M., and Klenk, H.-P. (2014) Genome sequence of gammaproteobacterial Pseudohaliea rubra type strain DSM 19751, isolated from coastal seawater of the Mediterranean Sea. *Genome Announc* **2**: e01208–e01214.

Spring, S., Scheuner, C., Göker, M., and Klenk, H.-P. (2015) A taxonomic framework for emerging groups of

ecologically important marine gammaproteobacteria based on the reconstruction of evolutionary relationships using genome-scale data. *Front Microbiol* **6**: 281.

Steinberg, S., Grinberg, M., Beitelman, M., Peixoto, J., Orevi, T., and Kashtan, N. (2021) Two-way microscale interactions between immigrant bacteria and plant leaf microbiota as revealed by live imaging. *ISME J* **15**: 409–420.

Steward, K.F., Eilers, B., Tripet, B., Fuchs, A., Dorle, M., Rawle, R., *et al*. (2020) Metabolic implications of using BioOrthogonal non-canonical amino acid tagging (BONCAT) for tracking protein synthesis. *Front Microbiol* **11**: 197.

Stone, M., DeForest, J., and Plante, A. (2014) Changes in extracellular enzyme activity and microbial community structure with soil depth at the Luquillo Critical Zone Observatory. *Soil Biol Biochem* **75**: 237–247.

Taylor, J.B., Carrano, A.L., and Kandlikar, S.G. (2006) Characterization of the effect of surface roughness and texture on fluid flow—past, present, and future. *International Journal of Thermal Sciences* **45**: 962–968.

Thamdrup, B. (2000) Bacterial Manganese and Iron Reduction in Aquatic Sediments. In: Schink B. (ed), *Advances in Microbial Ecology*, (vol **16**). Boston, MA: Springer. https://doi.org/10.1007/978-1-4615-4187-5_2

Thompson, L.R., Sanders, J.G., McDonald, D., Amir, A., Ladau, J., Locey, K.J., *et al*. (2017) A communal catalogue reveals Earth's multiscale microbial diversity. *Nature* **551**: 457–463.

Tobias, C., and Neubauer, S.C. (2019) Salt marsh biogeochemistry—an overview. In *Coastal Wetlands*. Amsterdam, Netherlands: Elsevier, pp. 539–596.

Valsami-Jones, E., McLean, J., McEldowney, S., Hinrichs, H., and Pili, A. (1998) An experimental study of bacterially induced dissolution of K-feldspar. *Mineral Mag A* **62**: 1563–1564.

Wang, Q., Garrity, G.M., Tiedje, J.M., and Cole, J.R. (2007) Naïve Bayesian classifier for rapid assignment of rRNA sequences into the new bacterial taxonomy. *Appl Environ Microbiol* **73**: 5261.

Welch, S.A., and Banfield, J.F. (2002) Modification of olivine surface morphology and reactivity by microbial activity during chemical weathering. *Geochim Cosmochim Acta* **66**: 213–221.

West, S.A., Diggle, S.P., Buckling, A., Gardner, A., and Griffin, A.S. (2007) The social lives of microbes. *Annu Rev Ecol Evol Syst* **38**: 53–77.

Wilbanks, E.G., Jaekel, U., Salman, V., Humphrey, P.T., Eisen, J.A., Facciotti, M.T., *et al*. (2014) Microscale sulfur cycling in the phototrophic pink berry consortia of the Sippewissett Salt Marsh. *Environ Microbiol* **16**: 3398–3415.

Wilbanks, E.G., Salman-Carvalho, V., Jaekel, U., Humphrey, P.T., Eisen, J.A., Buckley, D.H., and Zinder, S. H. (2017) The green berry consortia of the Sippewissett salt marsh: millimeter-sized aggregates of diazotrophic unicellular cyanobacteria. *Front Microbiol* **8**: 1623.

Winter, J., Schindler, F., and Wildenauer, F. (1987) Fermentation of alanine and glycine by pure and syntrophic cultures of Clostridium sporogenes. *FEMS Microbiol Ecol* **3**: 153–161.

Wittebolle, L., Marzorati, M., Clement, L., Balloi, A., Daffonchio, D., Heylen, K., *et al*. (2009) Initial community evenness favours functionality under selective stress. *Nature* **458**: 623–626.

Wright, J.J., Konwar, K.M., and Hallam, S.J. (2012) Microbial ecology of expanding oxygen minimum zones. *Nat Rev Microbiol* **10**: 381.

Ye, R., Jin, Q., Bohannan, B., Keller, J.K., and Bridgham, S. D. (2014) Homoacetogenesis: a potentially underappreciated carbon pathway in peatlands. *Soil Biol Biochem* **68**: 385–391.

Ye, S., Zhang, Y., and Sleep, B.E. (2015) Distribution of biofilm thickness in porous media and implications for permeability models. *Hydrgeol J* **23**: 1695–1702.

Zhou, S., Tang, J., Yuan, Y., Yang, G., and Xing, B. (2018) TiO_2 nanoparticle-induced nanowire formation facilitates extracellular electron transfer. *Environ Sci Technol Lett* **5**: 564–570.

Supporting Information

Additional Supporting Information may be found in the online version of this article at the publisher's web-site:

Appendix S1: Supplementary Information.

Fig. S1. A schematic diagram indicating the sediment depth horizons from which the data sets presented in this study were derived. Please see the referenced Figures and Datasets for the results associated with each depth-specific analysis.

Fig. S2. Two representative fields of view from samples BM, CM, and AM, demonstrating the potential for false positive fluorescence microscopy signals. Brightness has been increased by 40% in all images.

Fig. S3. To test the effect of our fluid replacement approach on transport of microbial cells, 1-μm fluorescent beads were introduced to the overlying water and tracked through the core during the fluid replacement and embedding process. A representative field of view from each horizon of fluorescent bead quantification is shown here.

Fig. S4. Sampling site at Little Sippewissett salt marsh. A) A satellite image of the marsh acquired on October 6th, 2018 (Google Earth). The white box indicates the 'Berry Pool' shown in image B where the sampling was conducted. The white arrow indicates the direction in which image B was acquired. B) The 'Berry Pool', so named because of its high abundance of phototrophic pink berries, as seen on August 25th, 2018. The white arrow points to the site of sample acquisition on September 26th, 2018. C) A closer view of the sediment surface at low tide on September 26th, showing pink berries, organic surface cover, and sandy sediment. D) Custom-built sample chambers placed at the site of collection for incubation, shown at low tide. E) Incubation chambers in an anoxic chamber during a fluid replacement step of the protocol, following *in situ* incubation.

Fig. S5. FACS plots. A) Shows the no HPG control (sample CS) used to draw gates around the BONCAT positive (anabolically active) and BONCAT negative (inactive) cell fractions in the HPG-amended sediment core (sample BS, panel B). Note that the biomass extracted from the the no HPG

control (A) was much lower than seen in other samples where HPG was added.

Fig. S6. Alpha diversity metrics of the bulk, BONCAT+ (Cy5+), and BONCAT- (Cy5-) communities analysed by 16S rRNA gene amplicon sequencing for each sediment horizon.

Fig. S7. Beta diversity metrics derived from 16S rRNA gene amplicon sequence data. A) Non-metric multidimensional scaling (NMDS) plot comparing bulk community with active/inactive sorted communities (stress 0.0784916). B) NMDS plot showing differences in sorted active/inactive communities by depth (stress 0.1517008).

Fig. S8. Representative fluorescence microscopy fields of view of *E. coli* cultures exposed to different concentrations of HPG and the azide dye and stained with the general DNA stain DAPI. In all panels, DAPI signal is shown in blue and the azide dye is shown in red. The 50 µM HPG, 5 µM dye combination provided the best combination of coverage and dynamic range and was used in the field-based experimental incubation.

Fig. S9. A comparison of BONCAT signal intensity when the azide dye reaction was conducted on the benchtop (oxic conditions) and in the anoxic chamber. Three random fields of view are shown; in all cases, images depict *E. coli* cells using 50 µM HPG, 5 µM dye, 60 min incubation, and dark conditions.

Fig. S10. The percentage of Sippewissett biomass that was anabolically active as a function of incubation time. All incubations used homogenized sediment from the 0–5 cm horizon, and received 50 µM HPG. Active and inactive organisms were quantified from fluorescence microscopy images as described in the text. Data points represent mean and standard deviation values across 5 fields of view; one field of view is provided for 1, 44, and 88 h below the graph to convey the full dynamic range of BONCAT-positive biomass proportions. For each image set, the left panel shows objects stained with SYBR green (indicative of all biomass), and the right panel shows objects stained with the Cy3

picolyl azide dye (indicative of the HPG-incorporating, anabolically active biomass). The brightness and contrast of each image has been increased by 40% to enhance visibility.

Fig. S11. The X-Ray diffractogram of bulk 0–8 cm homogenized Sippewissett sediment.

Fig. S12. To co-register fluorescence and electron microscopy images and facilitate precise spatial analysis, the bUnwarpJ algorithm in FIJI / ImageJ was used. See the text for details on parameter settings.

Fig. S13. To determine the z-axis depth into the embedded section that our protocol would detect, Cy3 (BONCAT) and SYBR green (all cells) channels were recorded at multiple focal depths with a step size of 0.35 µm. Three BONCAT and two SYBR green features are highlighted. Each resulting image was processed identically, as described in the text; Cy3 signal was colour-shifted to yellow and SYBR green signal was colour-shifted to blue for viewing ease. Features that registered as an 'object' after processing have a yellow or blue border; those that were not have no border. For each feature, the depth-based analysis began when the object was fully in focus.

Fig. S14. Histograms of the number of organisms as a function of distance from mineral surfaces. Histogram bins are in increments of 5 µm; the number of each bin corresponds to the upper bound of the range (e.g., '5' includes all organisms between 0 and 5 µm from the mineral surface). Only organisms on the outside of mineral grains are shown. Mineral types with less than 83 associated cells (e.g., <1% of the total mineral-external cells observed in this study) are not shown.

Table S1. Details on the conditions and analyses to which experimental and control sediment cores were subjected.

Table S2. Ingredients of the M9 minimal medium used in this study.

Table S3. Ingredients of the dye solution used in this study.